Magneto-structural and photocatalytic behavior of mixed Ni–Zn nano-spinel ferrites: visible light-enabled active photodegradation of rhodamine B

Published: 31 May 2020

Volume 31, pages 11352–11365, (2020) Cite this article

Journal of Materials Science: Materials in Electronics

Aims and scope

Submit manuscript

Swapnil A. Jadhav, Sandeep B. Somvanshi, Mangesh V. Khedkar, Supriya R. Patade & K. M. Jadhav

Abstract

The present study compiles with the physicochemical, magnetic, and photocatalytic evaluation of the mixed spinel Ni–Zn nanoferrites prepared by the auto-combustion sol–gel

route. All the samples were characterized by XRD for the recognition of phase-pure cubic spinel structure. Spectral studies that were carried out by FT-IR clearly show two absorptions band revealing the characteristics of ferrite skeleton. The morphology of the prepared nanoparticles was visualized by SEM and TEM microscopy technique. BET analysis showed the enhancement in surface parameters. Hydrodynamic diameter and dispersion studies were evaluated by DLS and Zeta potential measurements. The DC resistivity measured by two-probe technique shows the semiconductor behavior for all the samples. M–H hysteresis loop of all the samples exhibited the superparamagnetic behavior. The energy bandgap values obtained by the UV–Vis spectroscopy technique show the increasing trend from 1.82 to 2.07 eV with increase in Ni^{2+} content. The photocatalytic activity of Rhodamine B was evaluated under sunlight irradiation. With increasing Ni^{2+} concentration, the degradation efficiency increased to 98%. Further, the present nanocatalyst shows active reusability and can be easily separable due to its magnetic nature. The obtained results show the enhanced photocatalytic of the Ni–Zn nanoferrites under the visible light in contrast with the available literature reports.

1 Introduction

Nowadays, the occurrence of toxic organic pollutants due to the development of industries has great effects on the clean environment such as the growth of plants, sea-animals, the fertility of the soil, and human health, therefore it is a serious global issue [1]. Over the past decade, young researchers focused on to synthesis of low-dimensional nanomaterials and widely used them in photocatalytic degradation of highly toxic organic pollutants [2]. Many researchers already concluded that low-dimensional materials have large surface area, active adsorptions sites, and electron–hole recombination rate under UV and visible light sources [3]. Rhodamine B is a chemical dye having structure as depicted in Scheme 1. It is generally used in industrials purposes like textiles, paints, paper, biotechnology applications such as fluorescence microscopy, flow cytometry, etc. [4]. The organic dyes may cause serious environmental problems related to eye, skin, and lung tract irritation [5]. So, eliminating dye from water is the most important and demanding task.

Scheme 1

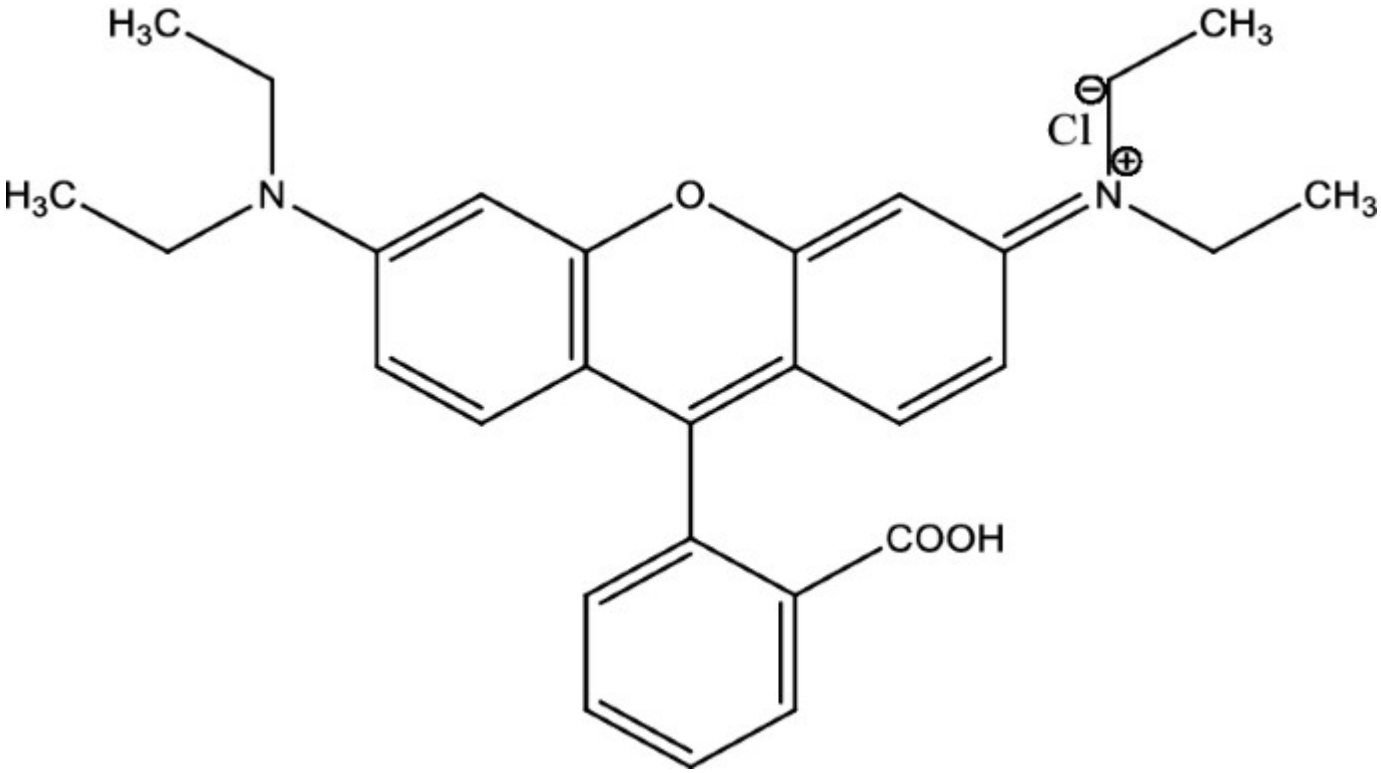

Structure of Rhodamine B

For the wastewater treatment, advanced oxidation process (AOPs) is the best alternative technique in comparison to adsorption, precipitation, and filtration for the degradation of organic pollutants [6]. The AOPs are very simple to operate eco-friendly with high efficiency and nonselective process. Generally, the Photocatalytic process is one of the types of AOPs procedure that is widely used for wastewater treatment. AOPs mainly includes the production of nonselective as well as enormously reactive hydroxyl radical (·OH). Hydroxyl radical can be formed by the interaction of Fe^{3+}/Fe^{2+} ions with H_2O_2, where H_2O_2 works as an oxidizing agent and Fe^{3+}/Fe^{2+} as catalyst [7,8,9].

Spinel ferrite nanomaterials offer photocatalytic properties, which are useful in various degradation of organic pollutants in wastewater [10]. The general formula of spinel ferrite nanoparticles is AFe_2O_4 (A can be Mn, Mg, Ni, Zn, etc.) [11,12,13] where A and Fe are metal cations which occupy tetrahedral and the octahedral sites, respectively [14,15,16]. Spinel ferrite nanoparticles are very useful in various bio-applications and electronic industries [17,18,19]. The nanostructured spinel ferrite samples can be prepared by diverse wet chemical routes viz. coprecipitation [20, 21], sol–gel auto-combustion [22,23,24], hydrothermal [25], solvothermal [26], sonochemical [27], etc. In the wet chemical method, the sol–gel auto-combustion method is more appropriate for the preparation of spinel ferrite nanoparticles, because of its simplicity, chemical homogeneity, low synthesis temperature, and environmentally approachable [28, 29]. Sivakumar et al. [30] prepared $NiFe_2O_4$ nanoparticles by sol–gel auto-combustion method using citric acid and obtained average particle size 8 nm with saturation magnetization of 50.4 emu/g. Lynda et al. [31] reported preparation of $Mg_{1-y}Ni_yFe_2O_4$ nanoparticles by sol–gel auto-combustion method using urea as reducing agent. P. P. Hankare et al. [32] successfully prepared $Co_{1-x}Ni_xFe_2O_4$ nanoparticles by sol–gel auto-combustion method. In the present work, structural, morphological, magnetic, and photocatalytic activity was improved with doping of Ni^{2+} into $ZnFe_2O_4$. The series of mixed spinel ferrite nanoparticles with chemical formula as $Ni_xZn_{1-x}Fe_2O_4$ (x = 0.0, 0.2, 0.4, 0.6, 0.8, 1.0) is reported with photocatalytic activity against Rhodamine B dye degradation under sunlight.

2 Experimental

2.1 Materials

All the chemicals such as nickel nitrate (Ni $(NO_3)_2{\cdot}6H_2O$), zinc nitrate (Zn $(NO_3)_2{\cdot}6H_2O$, 98%), ferric nitrate (Fe $(NO_3)_3{\cdot}9H_2O$), urea ($CO(NH_2)_2$), ammonia (NH_3), hydrogen peroxide (H_2O_2), Rhodamine B ($C_{28}H_{31}ClN_2O_3$), and deionized water were purchased from Fisher scientific Pvt. Ltd. and used for the synthesis of the nanoparticles.

2.2 Preparation

The series of Ni–Zn nanoparticles in powder form was prepared by the sol–gel technique consisting of auto-combustion under the assistance of Urea as a chelating agent. All ferric nitrate, nickel nitrate, zinc nitrate, and urea were dissolved in 300 ml deionized water with nitrate-to-fuel ratio as 1:4. Then the pH was maintained at 7 using ammonia. The solution mixture was stirred continuously at a constant temperature (80 °C) to form a viscous gel. The temperature was then increased up to 120–140 °C for the combustion process. The combustion was taking place and the fluffy powder was formed. The synthesized powder was sintered at temperature 650 °C for 360 min using a muffle furnace. The synthesized samples were coded as $ZnFe_2O_4$, $Ni_{0.2}Zn_{0.8}Fe_2O_4$, $Ni_{0.4}Zn_{0.6}Fe_2O_4$, $Ni_{0.6}Zn_{0.4}Fe_2O_4$, $Ni0_{.8}Zn_{0.2}Fe_2O_4$, $NiFe_2O_4$, respectively.

2.3 Photocatalytic degradation measurement

The prepared series of Ni–Zn nanoparticles was used for the degradation of Rhodamine B under solar light. All the experiments were carried out using double-distilled water. The temperature of the experimental reaction was found to be 30 °C to 37 °C. 0.5 g of prepared nanoparticle samples were mixed in 250 ml of 10 mg/l of RhB solution which was then kept in solar light. Earlier, the solution was stirred for 30 min, and then the solution shows completely adsorption–desorption equilibrium between the prepared samples and RhB solution. Further, the 10 ml of hydrogen peroxide were added into the solution. At every given time interval, 3 ml RhB solution was taken out for the measurement. Before and after photocatalytic degradation, the RhB solution was measured using the UV–Vis spectroscopy technique. The decolorization efficiency of RhB was determined by the following equation [25],

$$\% D = \frac{{C_{{0}} - C_{t} }}{{C_{{0}} }} \times 100,$$

where C_0 is initial RhB concentration and C_t is the concentration of the dye after a time interval.

2.4 Characterization

The thermal degradation process was estimated through the thermal gravimetric and different thermal analyses in the temperature range from room temperature to 600 °C in a nitrogen atmosphere using Shimadzu model. The X-ray diffraction patterns of the synthesized samples were observed through X-ray powder diffractometer (Advanced Bruker D8) in the 2θ range of 15–80° with Cukα radiation (1.5418 Å) at room temperature. The Fourier transform infrared (FT-IR) spectra of the synthesized samples were examine through PerkinElmer Spectrophotometer with range 350–4000 cm^{-1}. FE-SEM with EDX was used to study morphologies with the elemental composition of prepared samples. TEM microscopy was also employed to visualize the morphology and structure. The specific surface area, pore size, and pore volume of the synthesized sample were evaluated on the BET (Quantachrome model) [33]. DLS and Zeta potential measurements were carried out with the help of Zetasizer Malvern Panalytical Instrument. The DC electrical resistivity was measured by the two-probe technique. The *J*–*V* curves were recorded by the Keithley 2400[1]. The magnetic measurement of synthesized samples was examined with the help of a vibrating sample magnetometer (VSM) (Lakeshore model) technique with an applied magnetic field. The optical bandgap and photocatalytic measurements were studied using UV–Vis spectrometer (Avantes UV–Vis spectroscopy model).

3 Result and discussion

3.1 1TG-DTA analysis

The TGA–DTA curve of the typical $NiFe_2O_4$ sample is depicted in Fig. 1. The thermal analysis occurred in three different phases. They initial weight loss of 3.5% at 100–250 °C corresponds to the reduction of water molecules and -OH ions from the particle surface. In the second phase of temperature range 450–580 °C, the weight loss of 4.6% occurred due to the decomposition of the surfactant. For the further temperature range (320–700 °C), the weight loss of 6.24% occurred due to the formation of pure-phase spinel ferrite [34,35,36].

Fig. 1

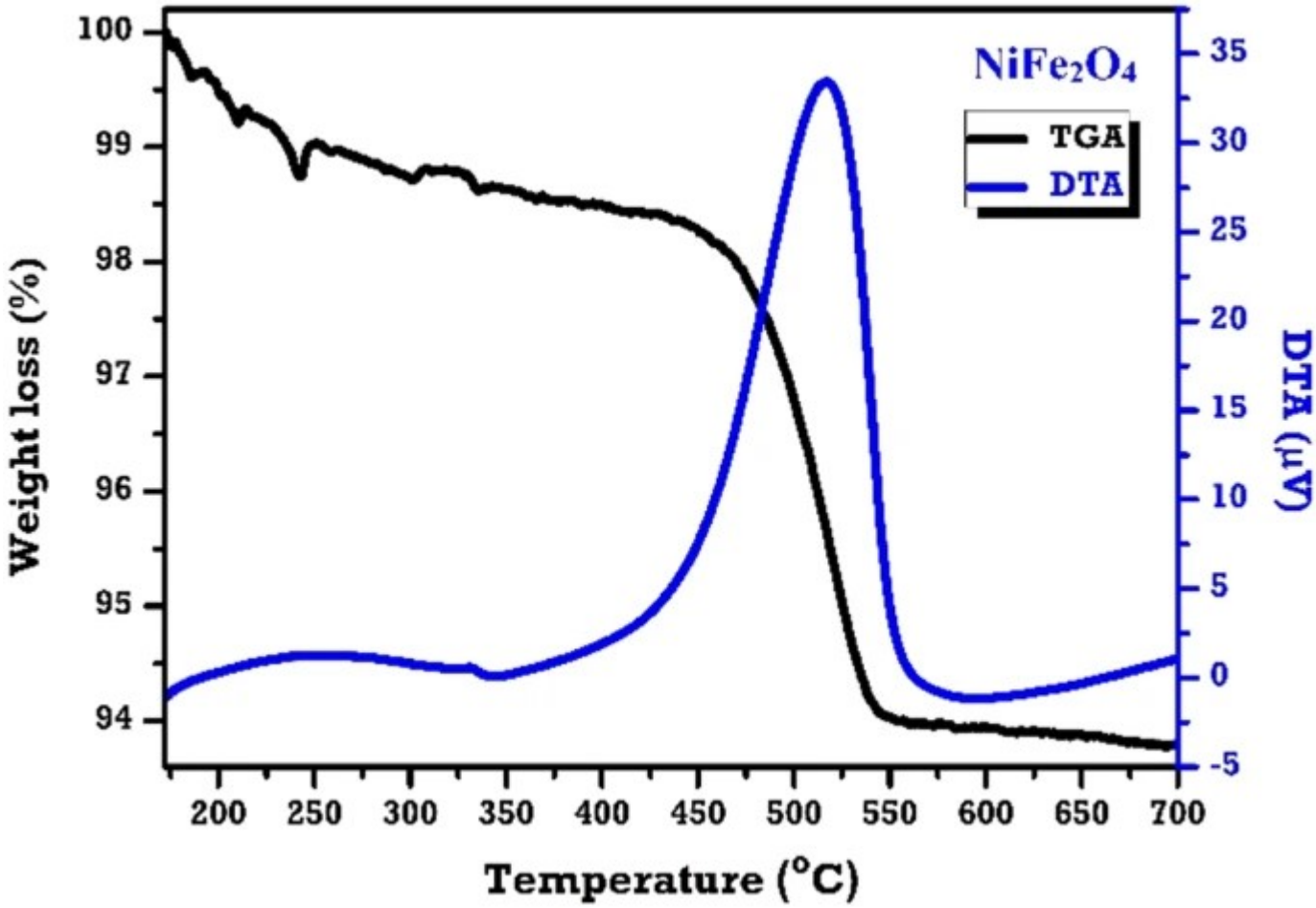

TGA and DTA curves of $NiFe_2O_4$ nanoparticles

3.2 XRD analysis

The XRD profile of the prepared series of Ni–Zn nanoparticles is depicted in Fig. 2a. The (*hkl*) planes of (111), (220), (311), (222), (400), (422), (511), and (440) confirm the formation of good crystallization with a single-phase spinel structure [12, 34, 37, 38].

Fig. 2

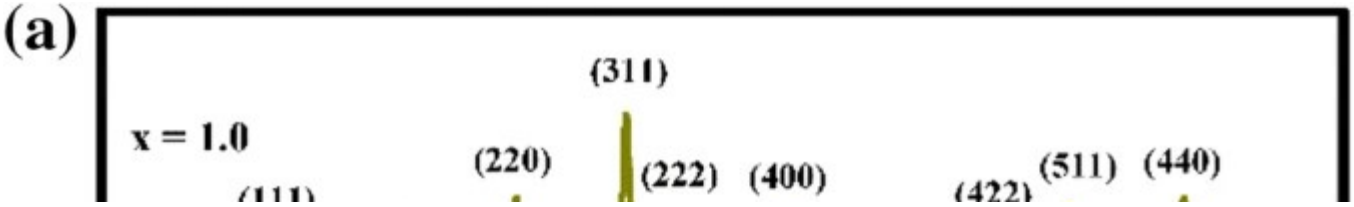

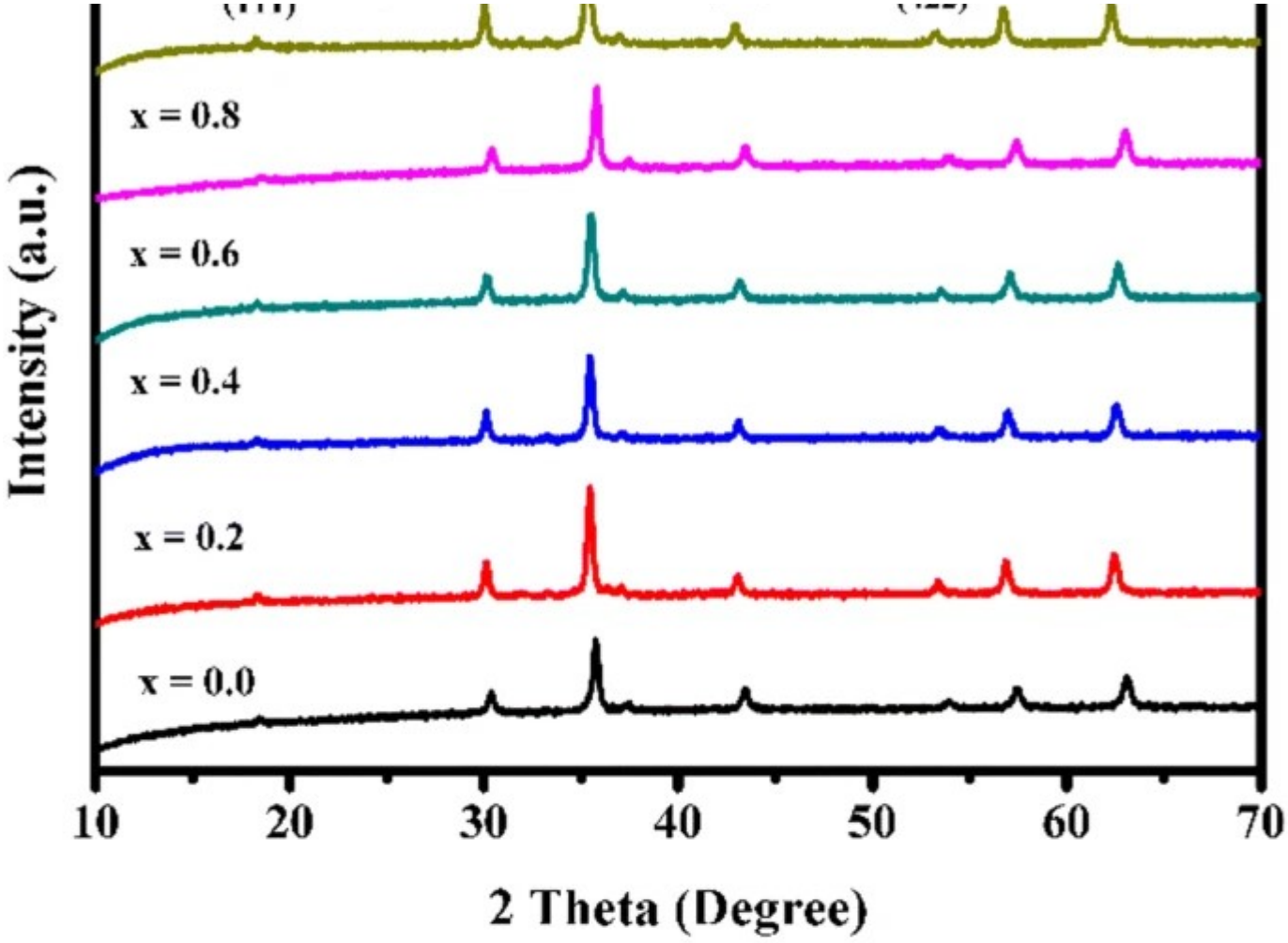
x = 0.8
x = 0.6
x = 0.4
x = 0.2
x = 0.0
Intensity (a.u.)
10
20
30
40
50
60
70
2 Theta (Degree)

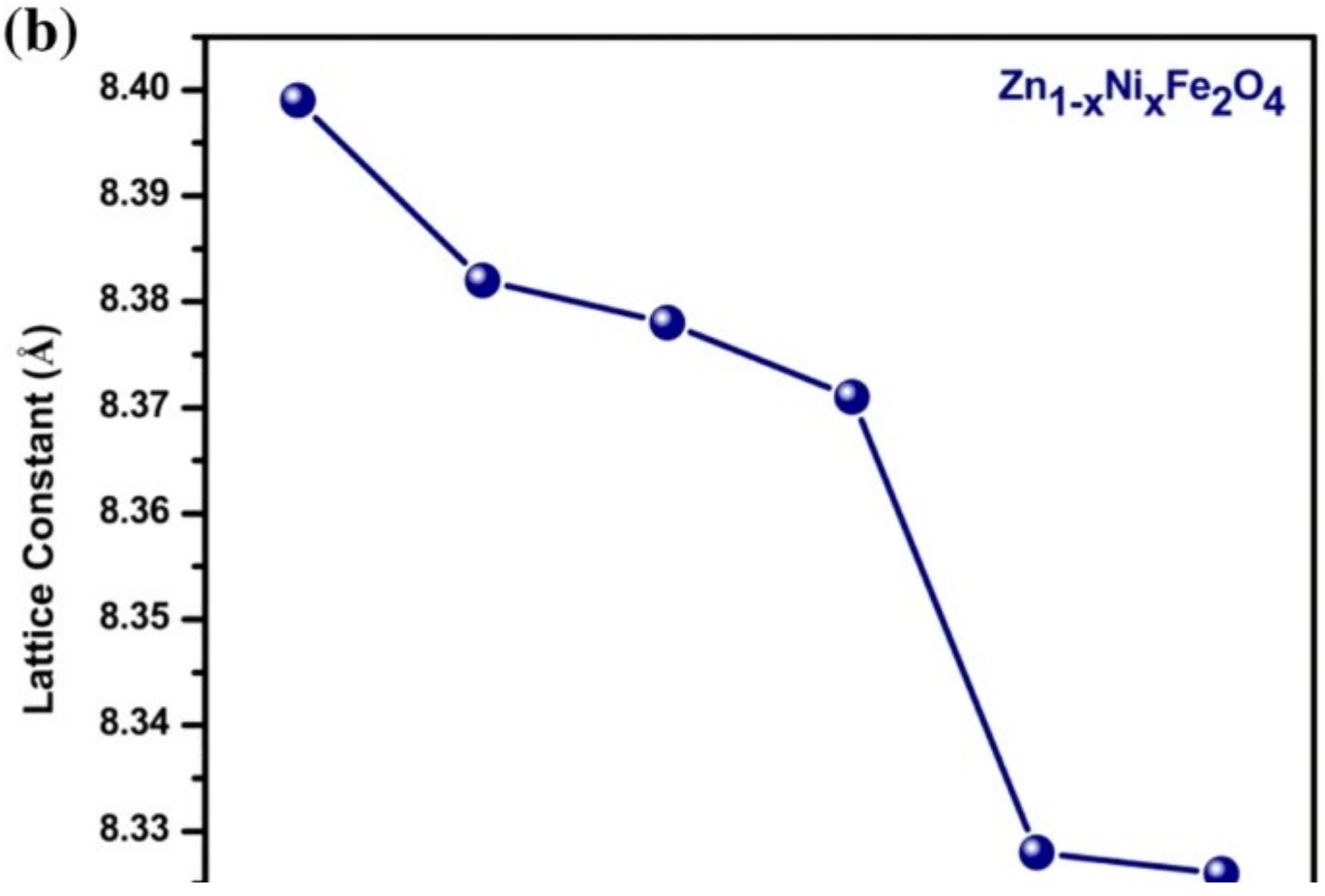
(b)
$Zn_{1-x}Ni_xFe_2O_4$
Lattice Constant (Å)
8.40
8.39
8.38
8.37
8.36
8.35
8.34
8.33

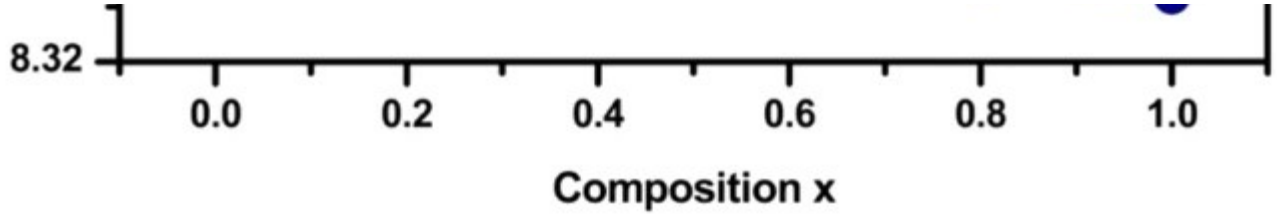

a XRD pattern of $Ni_xZn_{1-x}Fe_2O_4$ (x = 0.0, 0.2, 0.4, 0.6, 0.8, 1.0) nanoparticles. b Variation of lattice constant with Ni content

The average crystallite size of the synthesized samples was calculated by Scherrer's formula [39],

$$D = \frac{0.9\lambda }{{\beta \cos \theta }},$$

where D is the average crystalline size, λ is the wavelength (1.541 nm), β is the full width half maximum, and θ is the Bragg diffraction angle. The plane (311) was selected to measure the crystalline size of the prepared series of Ni−Zn nanoparticles. Table 1 shows that the crystalline size of the synthesized sample was decreased from 23 to 15 nm. Later, it is observed that urea has played an important part in controlling particle size. The lattice constant of synthesized nickel-doped zinc−ferrite nanoparticles was calculated using the Bragg equation [40],

$$a = d\,*\,(h^{2} + k^{2} + l^{2})^{1/2} ,$$

Table 1 Lattice constant, crystallite size of $Ni_xZn_{1-x}Fe_2O_4$ (where x = 0.0, 0.2, 0.4, 0.6, 0.8, 1.0) nanoparticles

where 'a' is the lattice constant, d is the Interplanar distance, and (h k l) is the miller indices. The lattice constant was increased with increasing Ni content in $ZnFe_2O_4$, due to the difference in ionic radius of Ni^{2+} (0.69 Å) and Zn^{2+} (0.72 Å) as shown in Fig. 2b. The calculated lattice constant values are also given in Table 1.

3.3 FT-IR analysis

The formation of functional groups was confirmed by Fourier transform infrared (FT-IR) spectroscopy. The FT-IR spectra of the prepared series of Ni–Zn nanoparticles are depicted in Fig. 3.

Fig. 3

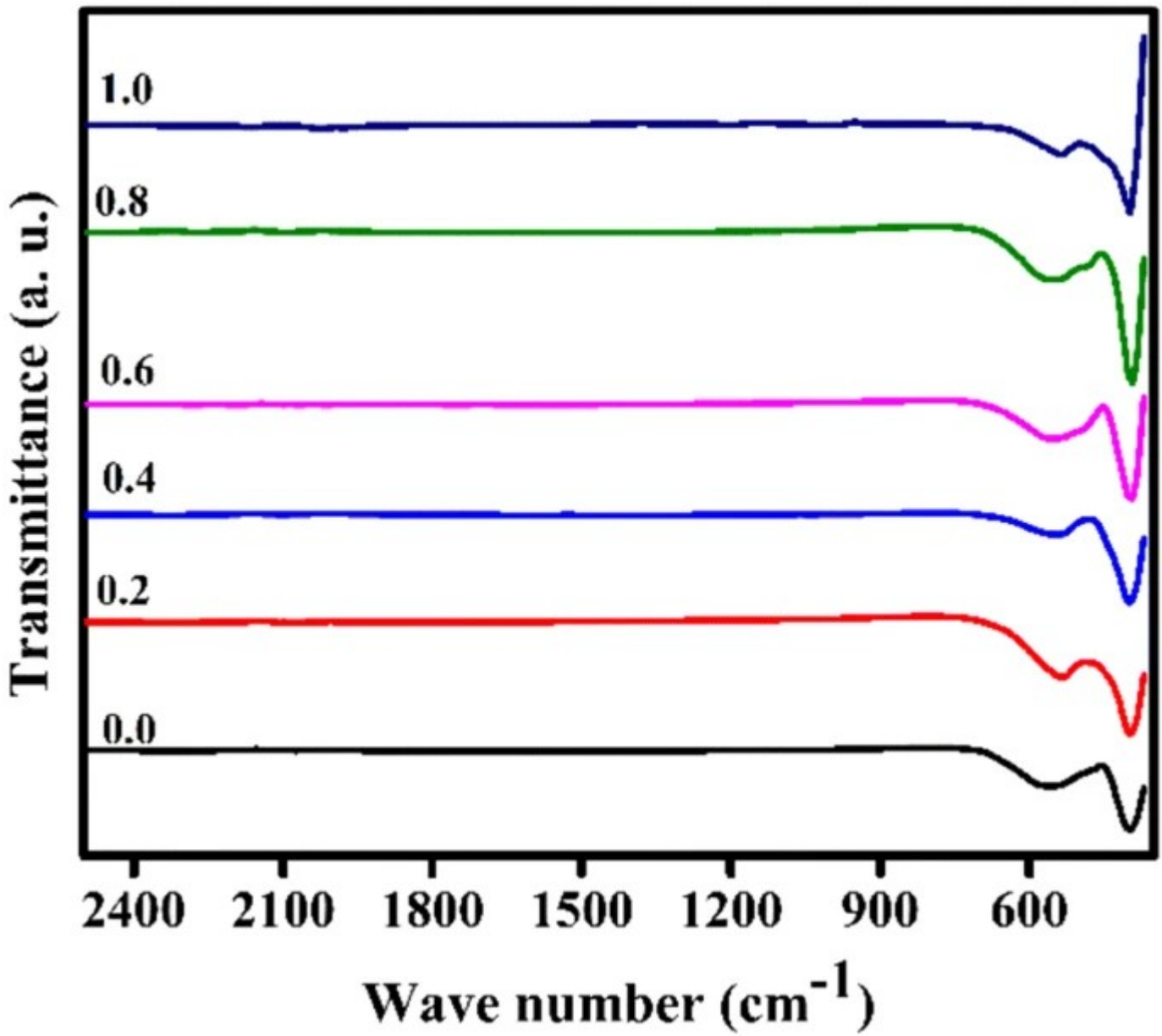

FT-IR spectra of $Ni_xZn_{1-x}Fe_2O_4$ ($x = 0.0, 0.2, 0.4, 0.6, 0.8, 1.0$) nanoparticles

Two metal–oxygen (M–O) vibration modes were revealed by FT-IR spectra within the range of 600 to 350 cm^{-1} confirming the successful formation of spinel ferrites. The first band (v_1) with the maximum frequency was observed in the range 576 to 532 cm^{-1} and the second band (v_2) with minimum frequency in the range 406 to 392 cm^{-1}, which indicates metal–oxygen stretching at tetrahedral (A) site and octahedral (B) site, respectively [41]. The first band υ_1 shifted towards higher wavenumber with increasing concentration of nickel and second band υ_2 decreases with increasing concentration of nickel in zinc ferrite which is shown in Table 2.

Table 2 Comparison of the FT-IR transmittance bands of Ni–Zn nanoparticles

3.4 FE-SEM and EDX analysis

The morphology of Ni–Zn nanoparticle samples was explored by using FE-SEM micrograph as depicted in Fig. 4. The result of FE-SEM images exposes that nanoparticles have found a closely arranged spherical shape with a dense population. The images show agglomeration because ferrite nanoparticles show the interaction of magnetic dipole. The average grain size of the prepared nickel-doped zinc ferrite nanoparticles was obtained as 18.45 nm and 15.85 nm. The EDX pattern of Ni-doped zinc ferrite (x = 0.4, 0.8) nanoparticles is shown in Fig. 4. The presence of iron, nickel, zinc, oxygen (no other extra peak) confirms the purity of prepared composition.

Fig. 4

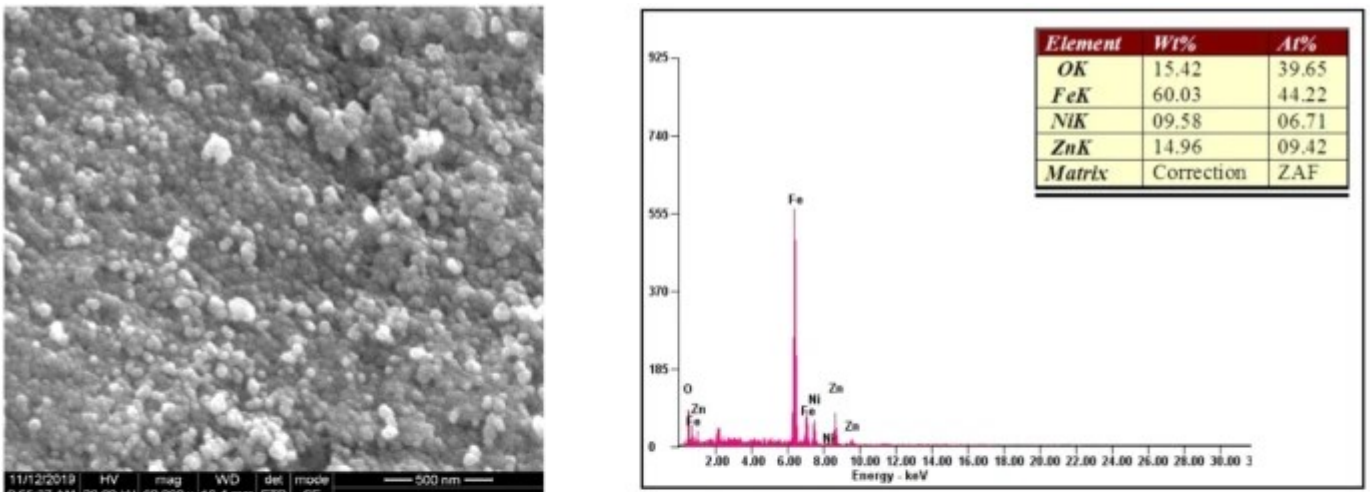

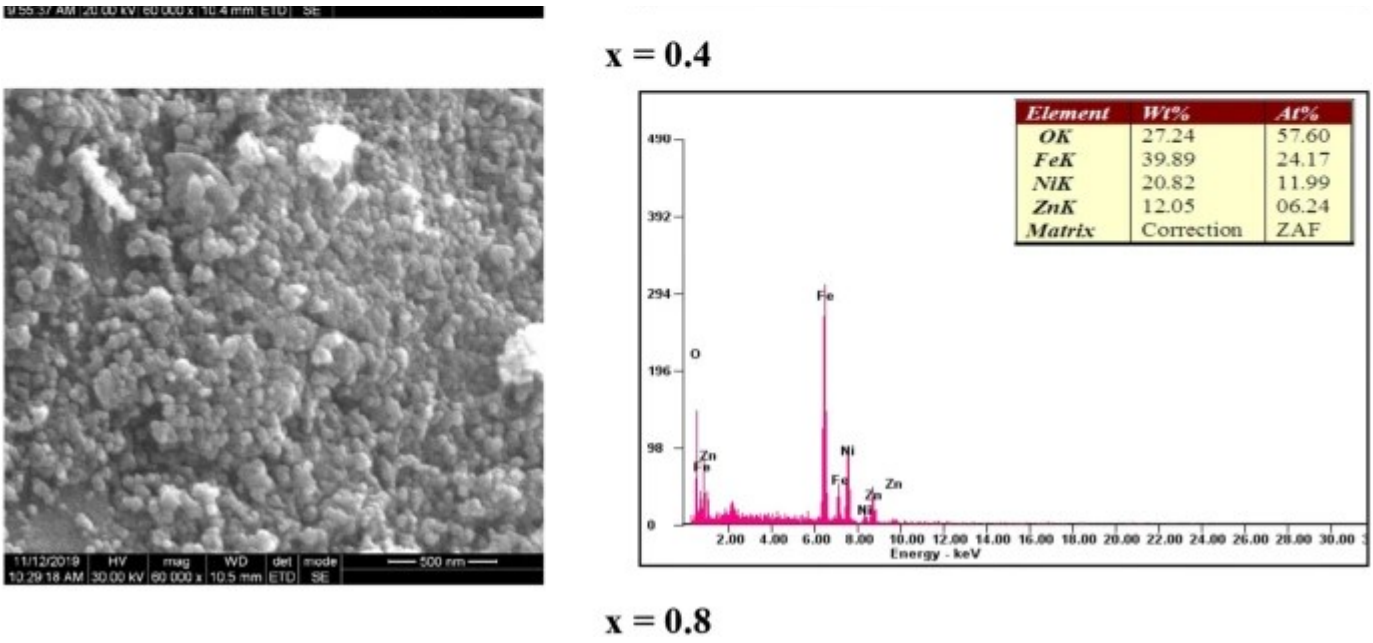

FE-SEM with EDX image of $Ni_xZn_{1-x}Fe_2O_4$ (x = 0.4, 0.8)

3.5 TEM analysis

Figure 5a, b shows the TEM micrograph and Fig. 5c, d shows the distribution of particle size determined from TEM results by fitting with the Gaussian distribution function for the typical samples of $Ni_xZn_{1-x}Fe_2O_4$ (x = 0.4 and x = 0.8). TEM images clearly show the spherical nature and uniform size of the particles. The diameter of 50 NPs was measured to determine the frequency of particle size which confirms average particle size as ~ 22 nm for x = 0.4 and ~ 13 nm for x = 0.8 samples, respectively. This result was nearly matching with average crystallite size determined by XRD analysis.

Fig. 5

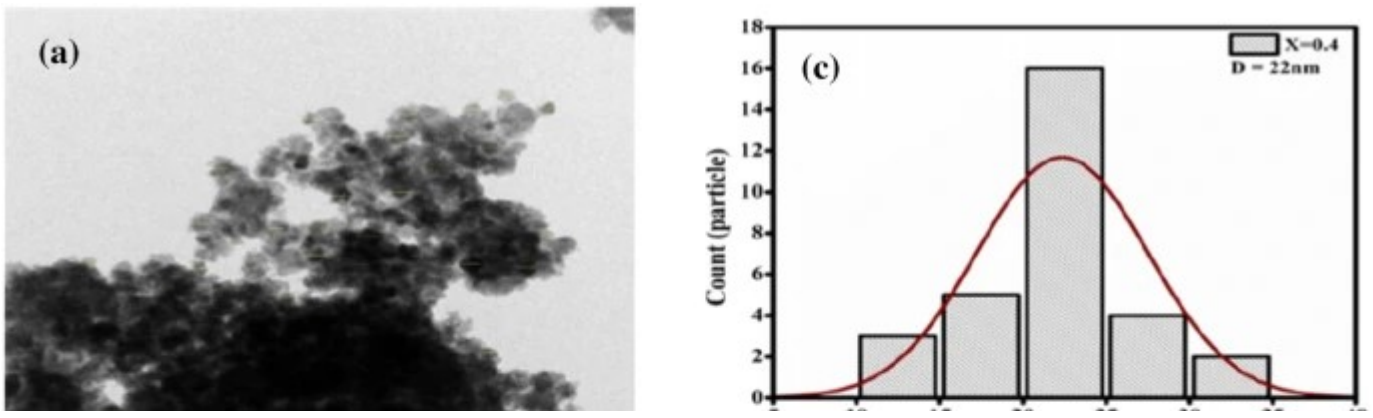

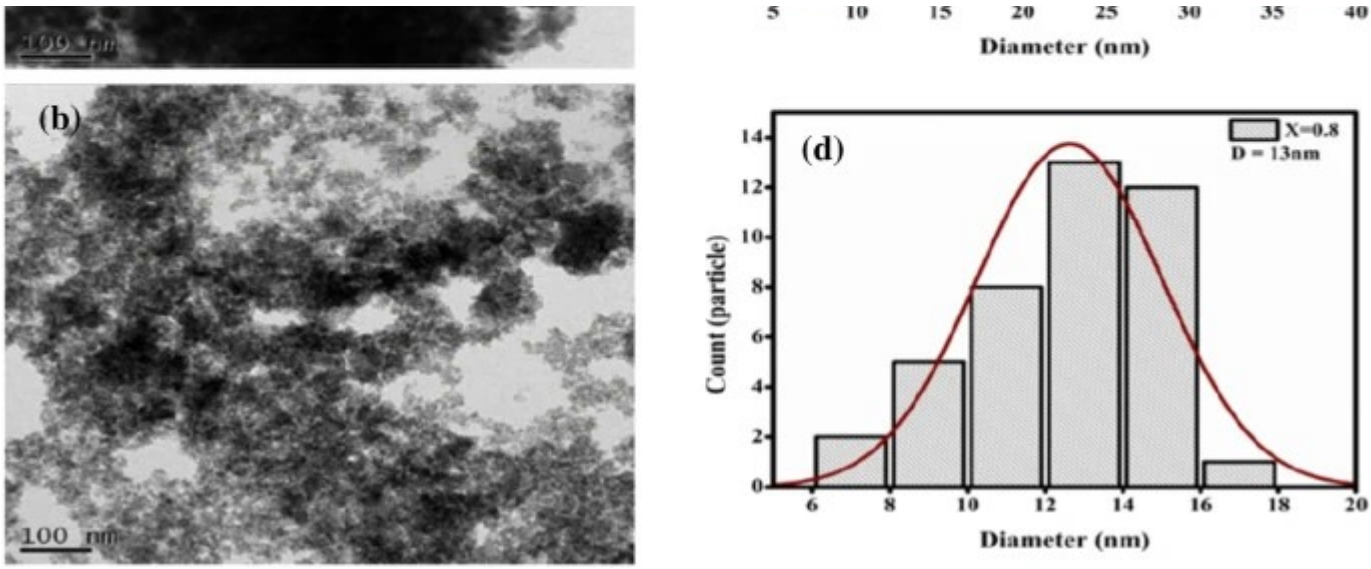

a, b TEM image and c, d particle distribution for $Ni_xZn_{1-x}Fe_2O_4$ ($x = 0.4, 0.8$) nanoparticles

3.6 BET surface area analysis

The N_2 adsorption–desorption isotherms of $NiFe_2O_4$, $Ni_{0.8}Zn_{0.2}Fe_2O_4$, $ZnFe_2O_4$ nanoparticles are depicted in Fig. 6. BET result demonstrated type IV hysteresis, which indicates the prepared materials are mesoporous in nature [42, 43]. Obtained BET results reveal that surface area increases with increase in nickel concentrations [44]. With decrease in particle size, the surface area was increased [45]. Table 3 shows the variation in pore volume and surface area for the typical samples. The enhanced surface parameters give evidence of improved photocatalytic activity of the prepared samples.

Fig. 6

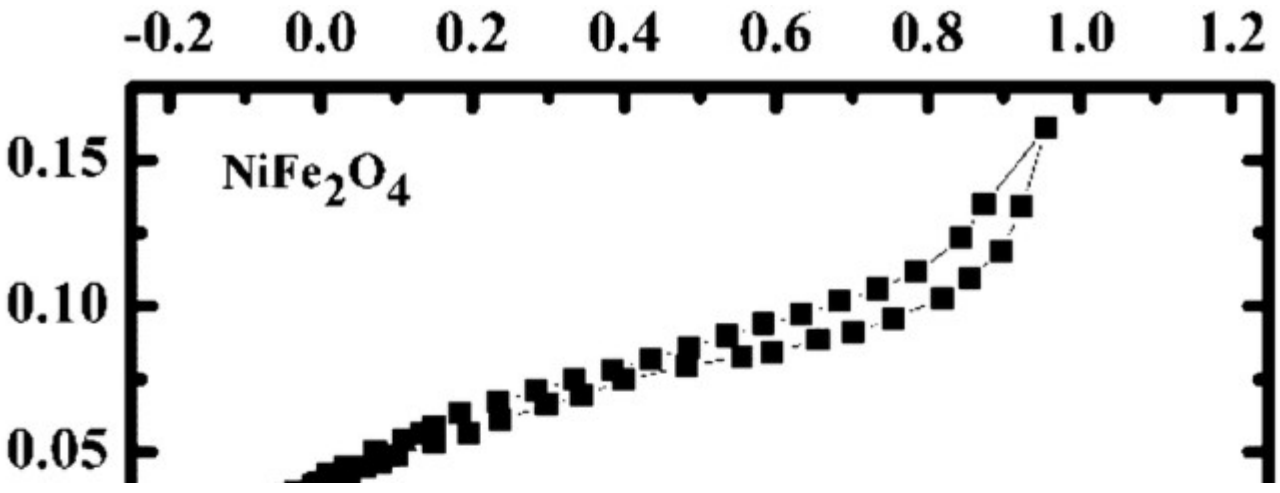

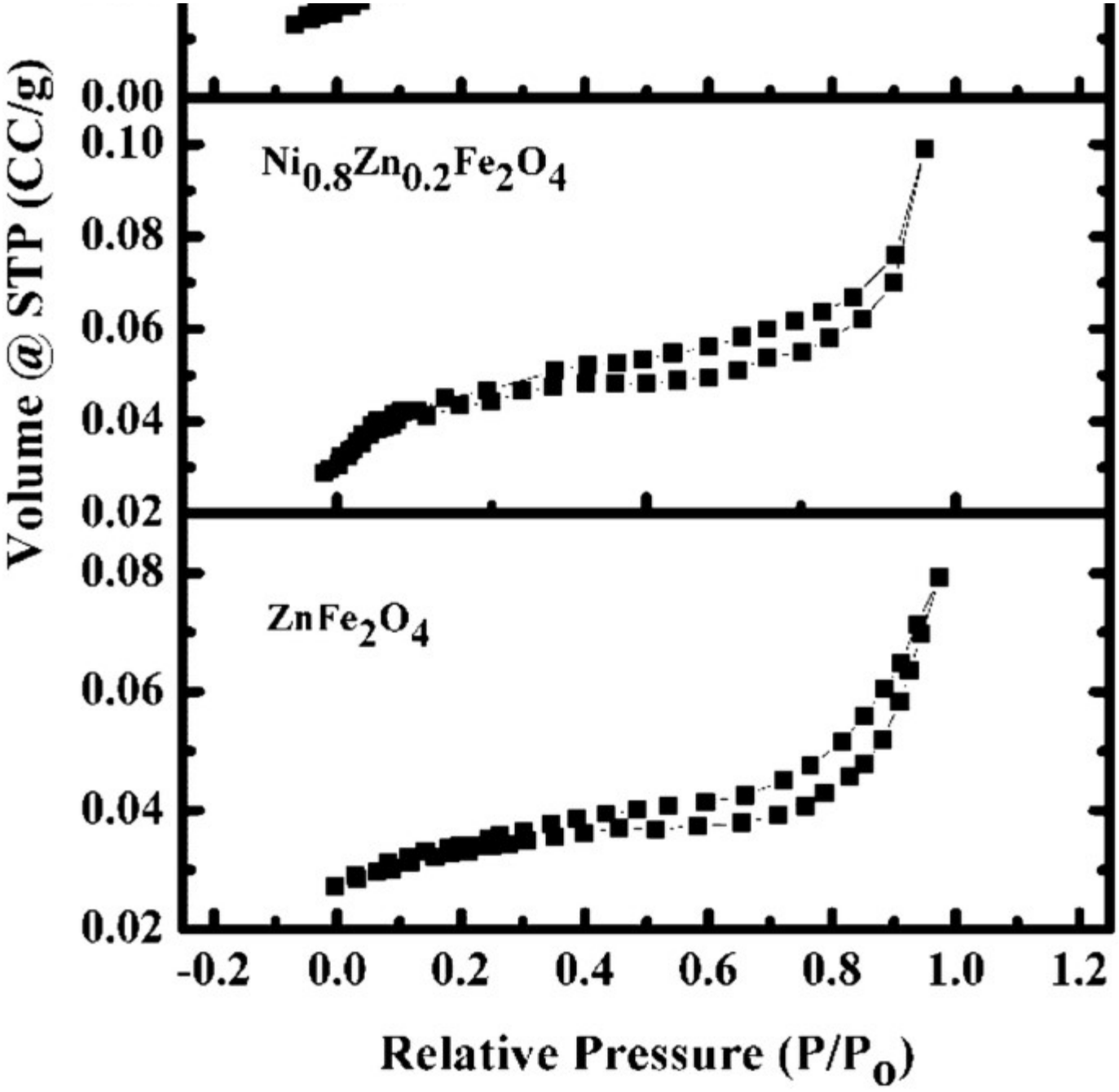

BET plot of $NiFe_2O_4$, $Ni_{0.8}Zn_{0.2}Fe_2O_4$, $ZnFe_2O_4$ nanoparticles

Table 3 Surface area, pore volume of $Ni_xZn_{1-x}Fe_2O_4$ (x = 0.0, 0.8, 1.0)

3.7 Dynamic light scattering (DLS) and zeta potential

DLS is a popular technique to determine the hydrodynamic diameter (HDD) of the nanoparticles dispersed in a colloidal suspension. The distribution of HDD sizes for all the prepared samples is displayed in Fig. 7a. The HDD size of the prepared nanoparticles was found to be in the range of 51 to 95 nm. It is also noted that HDD sizes decreased with the increase in nickel substitution in zinc ferrite. This decrease in HDD size can be correlated with the decrement in crystallite size values. The highest size of HDD was found for the pristine zinc ferrite due to the inferior insoluble nature and agglomeration of particles in colloidal suspension. In addition to DLS, the Zeta potential was also measured for all the samples to know the charge on the surface and stability of the nanoparticles. Figure 7b displays the Zeta potential of nickel-substituted zinc–ferrite nanoparticles. The zeta potential values for all the samples are found in the range of ± 37 mV and ± 43 mV. The isoelectric points of all the prepared samples are found in the range of 5.57 to 6.77. The increase in the isoelectric point confirmed that the nickel substitution in zinc ferrite improves the colloidal stability of nanoparticles.

Fig. 7

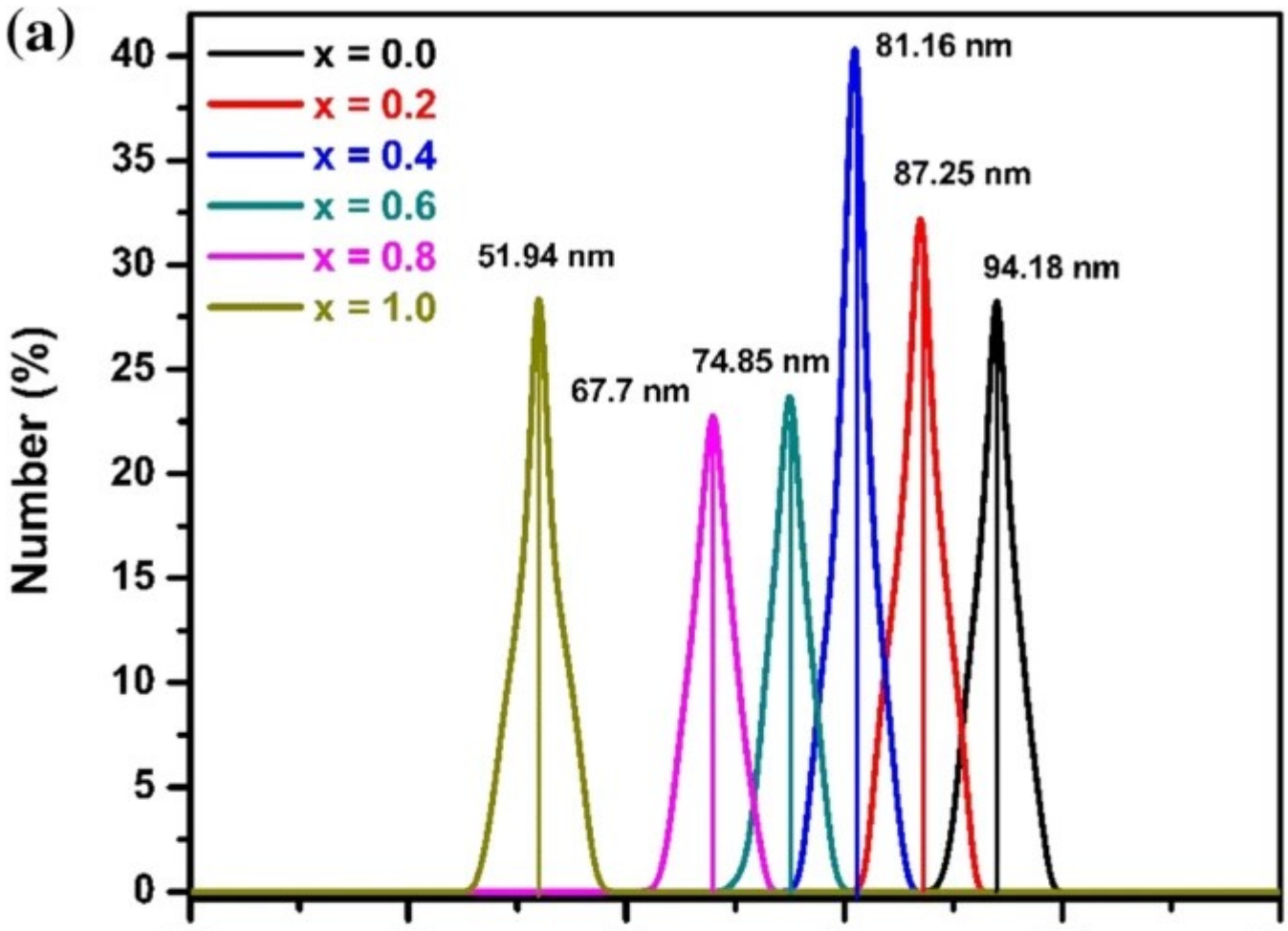

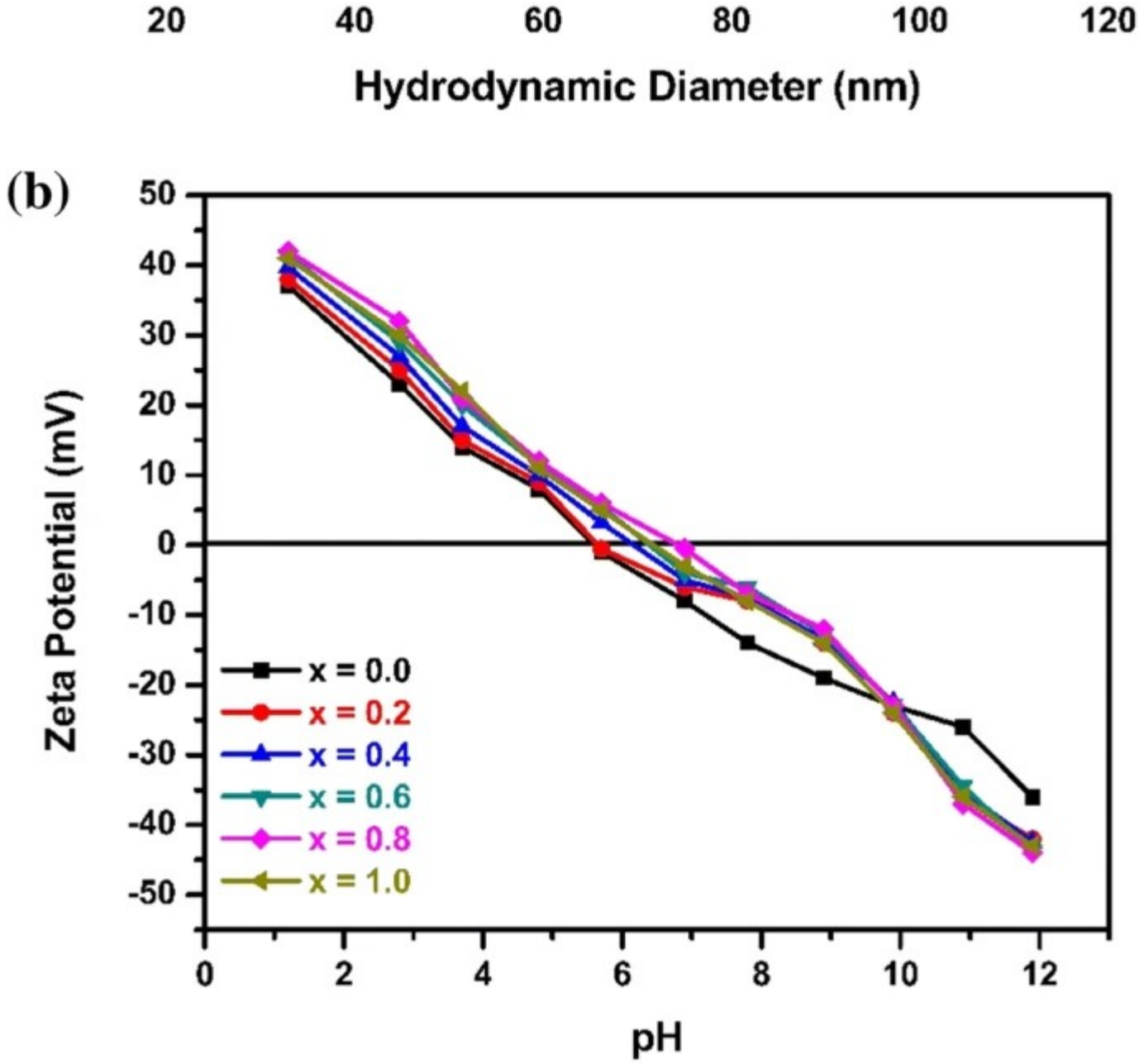

a Particles size distribution for $Ni_xZn_{1-x}Fe_2O_4$ (x = 0.0, 0.2, 0.4, 0.6, 0.8, 1.0) nanoparticles. b zeta potential as a function of pH for $Ni_xZn_{1-x}Fe_2O_4$ (x = 0.0, 0.2, 0.4, 0.6, 0.8, 1.0) nanoparticles

3.8 DC electrical resistivity analysis

The DC resistivity is a dynamic property of spinel ferrite to determine the electrical gesture. The resistivity of spinel ferrite nanoparticles can be influenced by sintering temperature, density, and the grain size. The resistivity of the spinel ferrites can be enhanced by substituting with proper trivalent or divalent ion to make them appropriate for desired applications. DC resistivity plots were drawn as log ρ versus 1000/T for $Ni_xZn_{1-x}Fe_2O_4$ (x = 0.0,

0.2, 0.4, 0.6, 0.8, 1.0) samples and are shown in Fig. 8a.

Fig. 8

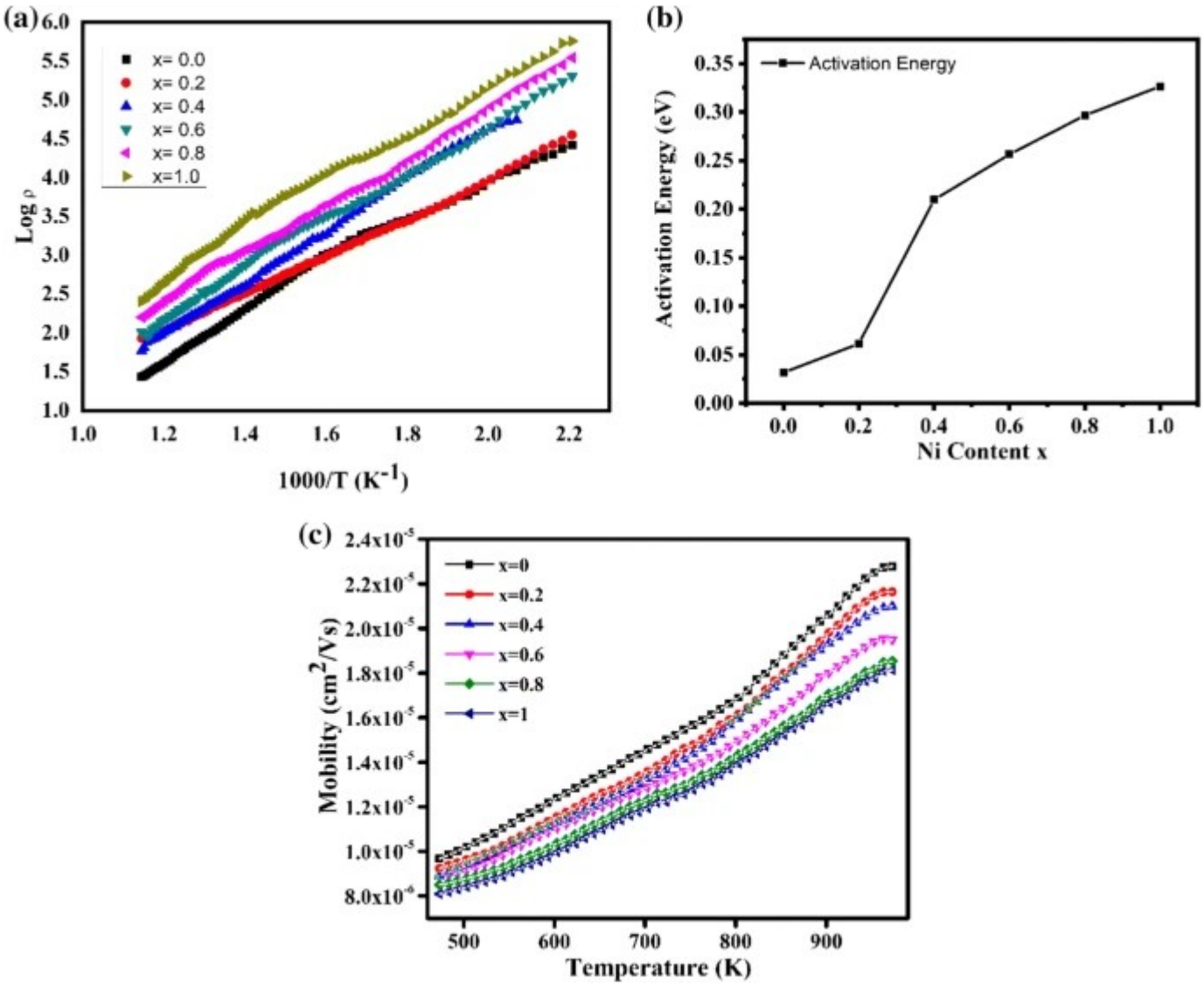

a DC electrical resistivity plot for $Ni_xZn_{1-x}Fe_2O_4$ (x = 0.0, 0.2, 0.4, 0.6, 0.8, 1.0) nanoparticles. b Activation energy as function of Ni Conc. for $Ni_xZn_{1-x}Fe_2O_4$ (x = 0.0, 0.2, 0.4, 0.6, 0.8, 1.0) nanoparticles. c Mobility as a function of temperature for $Ni_xZn_{1-x}Fe_2O_4$ (x = 0.0, 0.2, 0.4, 0.6, 0.8, 1.0) nanoparticles

It is observed from Fig. 8a that DC resistivity decreases with increase in temperature obeying Arrhenius relation which shows semiconducting behavior of all the samples. The decrease in DC resistivity with temperature can be attributed to the enhanced drift mobility. The charge

carriers are required for the hopping of electron between adjacent ions at octahedral sites which enhances the mobility of charge carries resulting in decrease in the resistivity and increase in the conductivity. The DC resistivity of the prepared samples increases with increasing Ni content. The activation energy for the prepared samples was calculated from the linear plot between log ρ and 1000/T using Arrhenius relation [46],

$$\rho = \rho_{0} e^{{\Delta E/K_{{\text{B}}} T}} ,$$

where ρ_0 represents room-temperature resistivity, k_B represents Boltzmann constant, and ΔE represents activation energy. The range of the activation energy for prepared samples increases with the increasing Ni concentration as shown in Fig. 8b [47].

The increase in activation energy shows that more energy is needed for electrons hopping due to Ni doping. The activation energy of prepared samples is shown in Table 4. The drift mobility of the prepared samples was calculated using the below relation [48] and is shown in Fig. 8c.

$$\mu_{{\text{d}}} = \frac{1}{ne\rho },$$

Table 4 Activation energy (ΔE), charge carrier concentration (n) (cm^{-3}), diffusion coefficient (D) cm^2/s, drift mobility (μ_d) $cm^2\ v^{-1}\ s^{-1}$

where μ_d is the drift mobility, e is the charge on electron, and ρ is the resistivity. Also, the values of the charge carrier's concentrations of prepared samples were calculated using the below relation [49]

$$n = \frac{{N_{{\text{A}}} D_{{\text{B}}} P_{{{\text{Fe}}}} }}{M},$$

where N_A represents Avogadro's number, D_B represents bulk density, P_{Fe} represents the number of Fe atoms, and M represents molecules mass of the corresponding chemical formula [50]. The calculated value of charge carrier concentrations is shown in Table 4.

It is observed by Hemeda et al. [51] that the diffusion of O^{2-} ions occurs by the defects in structural vacancies. For each structure, the diffusion coefficient of oxygen vacancies was determined using the resistivity data and the given equation [52],

$$D = \frac{{ \sigma k_{{\text{B}}} T}}{{Ne^{2} }},$$

where D is the diffusion coefficient, σ is the reciprocal of resistivity, k_B is the Boltzmann constant, T is the temperature, N is the number of atoms/cm^3, and e is the charge on the electron. Table 4 shows the variance of the diffusion coefficient at 473 K for all the prepared samples and it indicates that the diffusion decreases with an increase in temperature. It is clear from Table 4 that as a result of nickel doping, the diffusion coefficient decreases. It can be verified by the growth of nickel ions, resulting in the formation of cation vacancy and the decrease of oxygen vacancies in the sub-lattice.

3.9 UV–Vis spectroscopy analysis

The optical properties of the prepared series of Ni–Zn nanoparticles with different Ni^{2+} concentration were investigated by using UV–Vis spectroscopy. The bandgap (E_g) value was calculated using Kubelka–Munk function $F(R)$. The vertical axis of the Kubelka–Munk function is equivalent to the absorption constant (α). Therefore, α in the Tauc equation is replaced with Kubelka–Munk function, and the resulting equation is represented as [53],

$$F\left(R\right) = \alpha = \frac{{(1 - R)^{2} }}{2R},$$

where α is the absorption constant, $F(R)$ is Kubelka–Munk function, R is diffuse reflectance. The plot of $[F(R)h\nu]^2$ against $h\nu$ is depicted in Fig. 9a.

Fig. 9

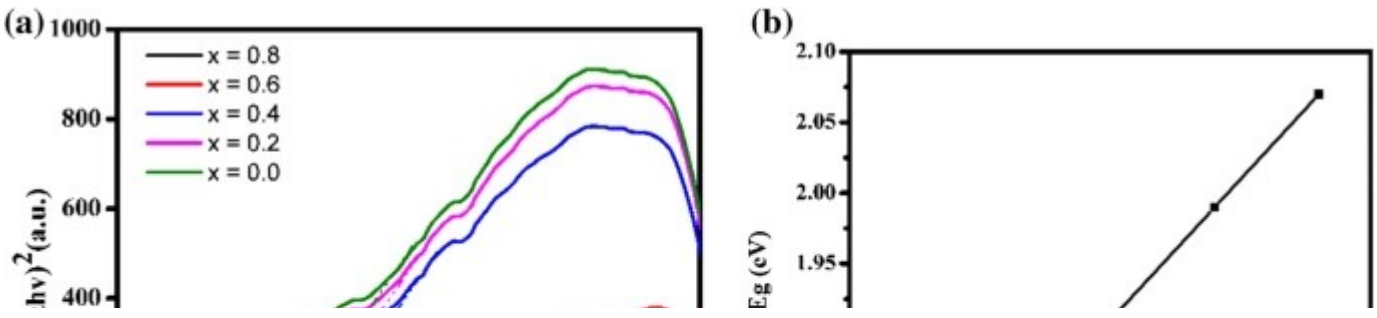

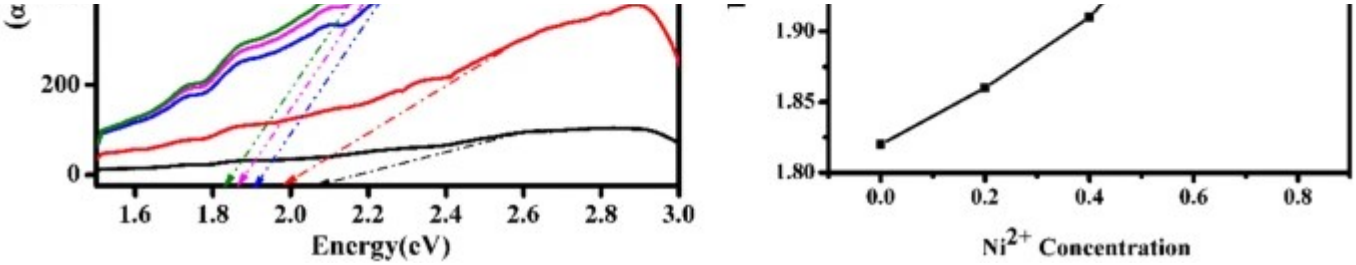

UV–Vis DRS of the prepared series of Ni–Zn nanoparticles (x = 0.0, 0.2, 0.4, 0.6, and 0.8), b variation of bandgap

The bandgap (E_g) values of the prepared Ni–Zn ferrite series were found to be 1.85, 1.86, 1.91, 1.99, and 2.07 eV, respectively. It was observed that the Ni^{2+} ions substitution in zinc–ferrite nanoparticles shows a significant effect on bandgap values. The bandgap (E_g) value of zinc ferrite is 1.85 eV, which increases with the Ni^{2+} concentration as depicted in Fig. 9b. This increase in bandgap values is attributed to the reduction of gain size (Quantum confinement effect) [54].

3.10 *J–V* analysis

Figure 10 shows current density versus voltage (J–V) plots of $Ni_xZn_{1-x}Fe_2O_4$ (x = 0.0, 0.2, 0.4, 0.6, 0.8, 1.0) nanoparticles for dark condition at 300 W/cm^2 intensities. Zinc–ferrite nanoparticles show a photosensitivity of ~ 86% which enhances to ~ 96% after Ni doping as estimated using below equation [55].

$$\% = \frac{R_d - R_l}{R_d} \times 100,$$

Fig. 10

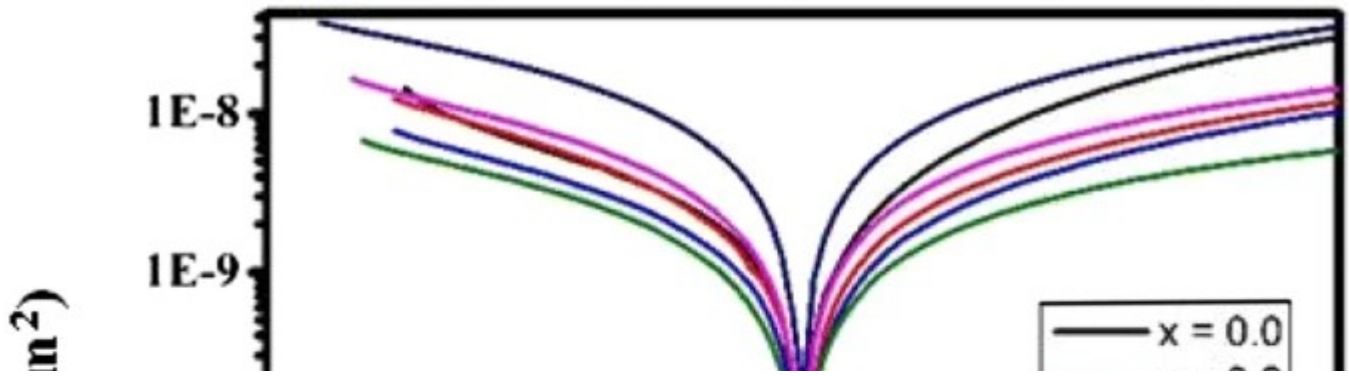

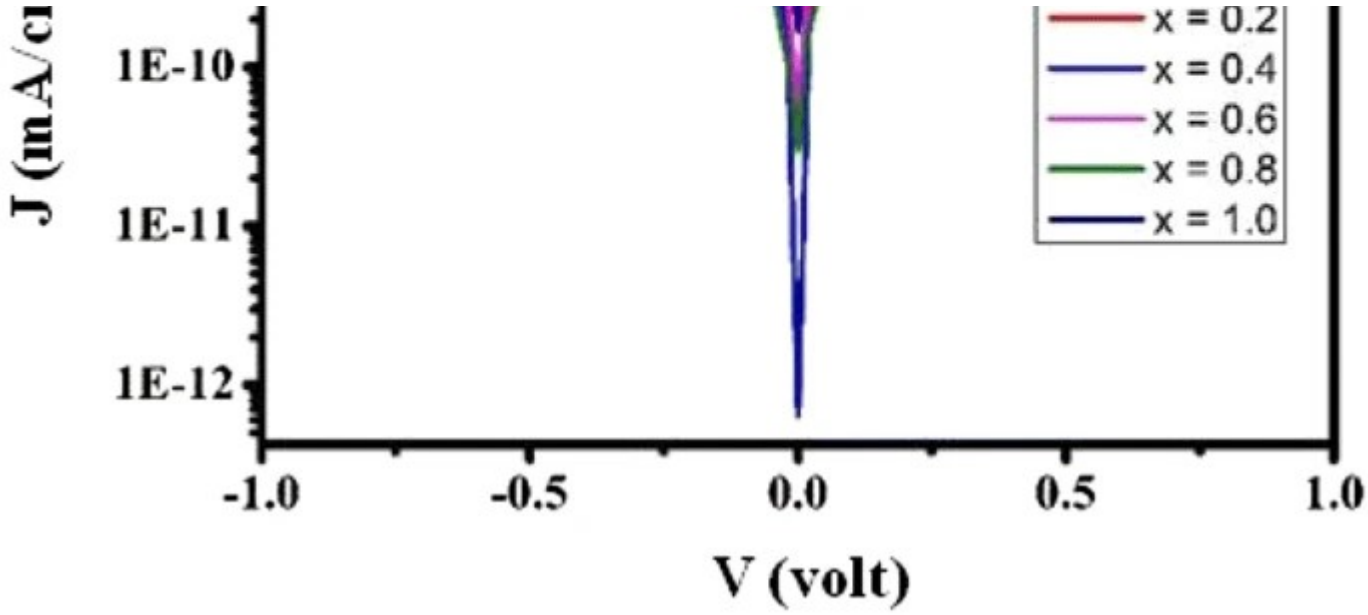

J–*V* plots of $Ni_xZn_{1-x}Fe_2O_4$ (x = 0.0, 0.2, 0.4, 0.6, 0.8, 1.0) nanoparticles

where S (%) is the photosensitivity, R_d is the resistance in dark, R_l is the resistance in light.

3.11 VSM analysis

Magnetic properties of the prepared samples were studied using a vibrating sample magnetometer and the respective *M*–*H* plots are depicted in Fig. 11a. The calculated value of saturation magnetization (M_s), remanence magnetization (M_r), coercivity (H_c), and Bohr magneton (μ_B) are shown in Table 5. The Bohr magneton number was calculated by using the following relation [56],

$$n = \frac{{M_{{\text{s}}} \times M_{{{\text{W}} }} }}{5585},$$

Fig. 11

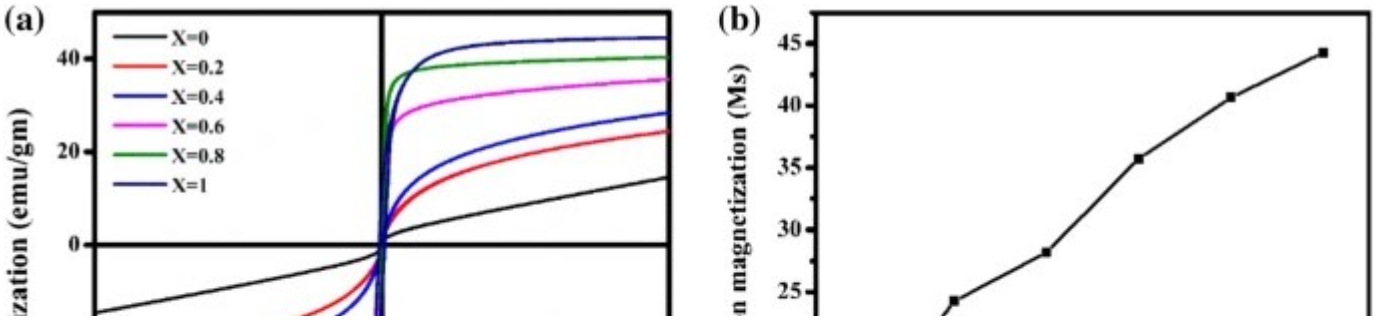

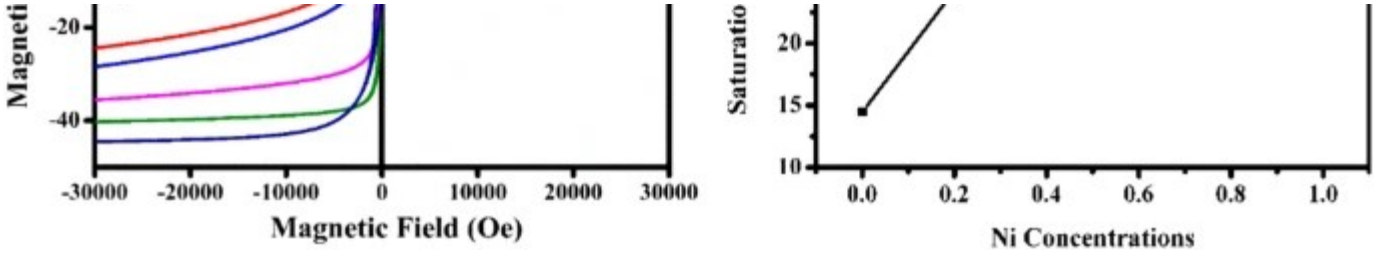

a Magnetization Hysteresis curves and b saturation magnetization Vs Ni concentration of $Ni_xZn_{1-x}Fe_2O_4$ (x = 0.0, 0.2, 0.4, 0.6, 0.8, and 1.0) nanoparticles

Table 5 Remanent magnetization (M_r), saturation magnetization (M_s), coercively (H_c), remanent ratio M_r/M_s, and magneto no. (n_B) for $Zn_{1-x}Ni_xFe_2O_4$ (x = 0.0, 0.2, 0.4, 0.6, 0.8, and 1.0) nanoparticles

where M_S is the saturation magnetization, M_W is the molecular weight of the sample, and n is the Bohr magneton number. By applying outside magnetic field, the prepared $NixZn_{1-x}Fe2O4$ (0.0, 0.2, 0.4, 0.6, 0.8, 1.0) photocatalyst can be separated from water and can be reused for degradation purposes.

Magnetic properties mainly depend on the particle size, distribution of cations, and doping. It was seen that all the magnetic parameters were increased with increasing nickel concentration in the zinc–ferrite matrix as shown in Fig. 11b. This increase in magnetic parameters was mainly due to the replacement of nonmagnetic zinc ions by magnetic Ni ions.

3.12 Photocatalytic activity

Photocatalytic properties depend on the surface area, particle size, and concentration of dopant materials and are most important factors that explain the photocatalytic activity [53, 57]. Padmapriya et al. [58] prepared zinc–ferrite nanoparticles for the photocatalytic activity of dyes and their degradation competence depends on surface area and particle size. Thus, we have compared undoped and nickel-substituted zinc–ferrite nanoparticles for the photocatalytic activity of Rhodamine B (RhB) under the sunlight.

3.12.1 Effect of Ni concentration on degradation of dye

The control of Ni concentration on zinc–ferrite nanoparticles for the photocatalytic activity of Rhodamine B is depicted in Fig. 12. The degradation efficiency of RhB was very small for the pure zinc–ferrite nanoparticles. With an increase in Ni concentration, the photocatalytic activity also increases to 90.23%, 92.3%, 94.89%, 97.56%, and 98.48% respectively. The high degradation efficiency of $Ni_{0.8}Zn_{0.2}Fe_2O_4$, $x = 0.8$ was observed due to the high surface area and crystalline size of the this sample. The present study confirmed that the degradation efficiency of pure zinc–ferrite nanoparticles was enhanced by increasing the Ni concentration.

Fig. 12

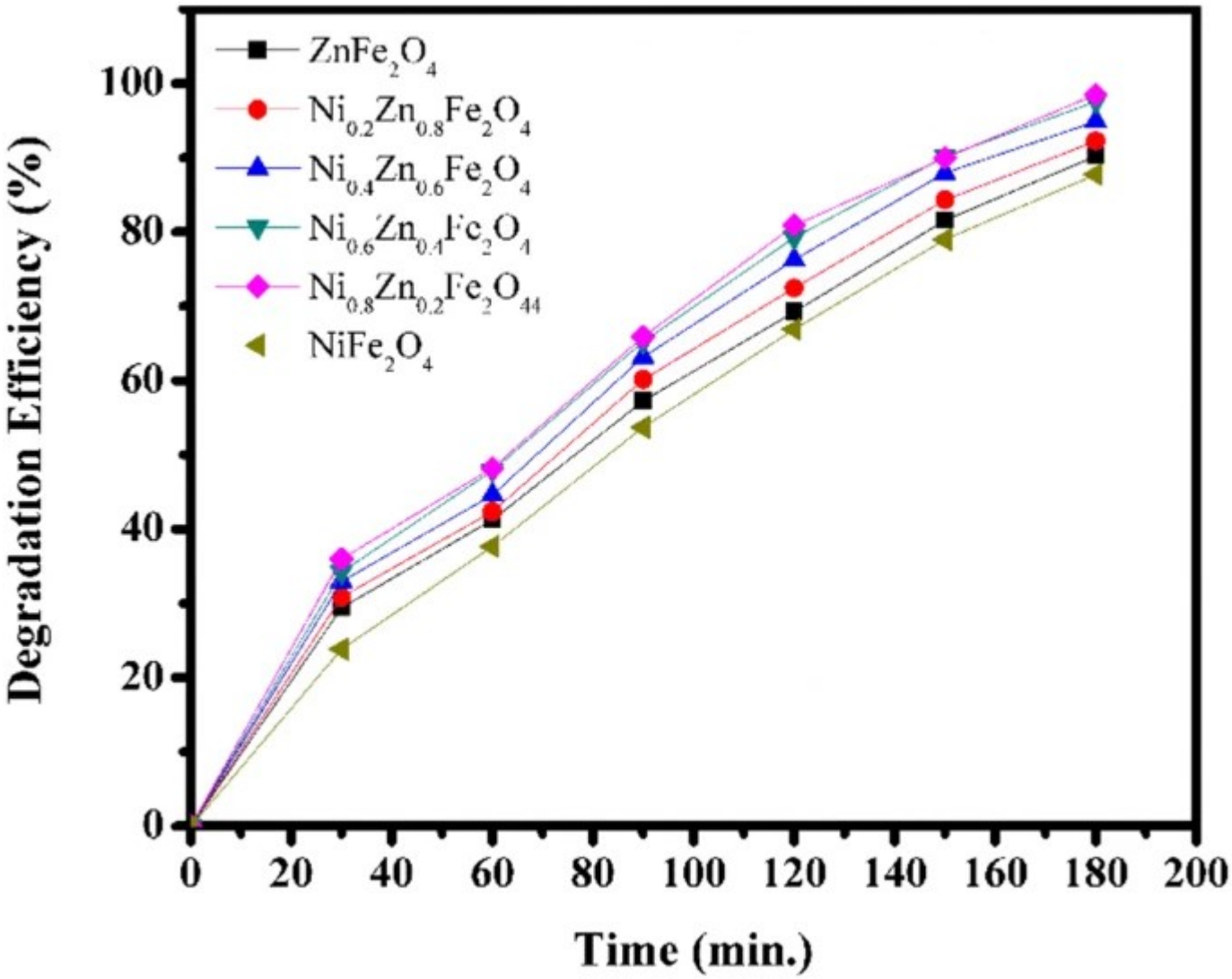

Effect of Ni concentration photocatalytic activity of $Ni_xZn_{1-x}Fe_2O_4$ ($x = 0.0$, 0.2, 0.4, 0.6, 0.8, and 1.0) nanoparticles

3.12.2 Effect of surface area on the degradation of dye

Materials with a high specific surface area are more effective on the degradation of dye for photocatalytic activity. When the surface area of the synthesized particles increases, the particle size decreases, whereas the electron–hole recombination rate enhances [57]. Surface area of $Ni_xZn_{1-x}Fe_2O_4$ with (x = 0.0, 0.2, 0.4, 0.6, and 0.8) nanoparticles are in the range of 2.2699 m^2/g to 4.4219 m^2/g and surface area of pure $NiFe_2O_4$ is 3.1100 m^2/g. The higher surface area was observed for sample with x = 0.8. This result shows that surface area enhanced the number of active sites in the sample. It indicates that x = 0.8 samples show good photocatalytic activity because of the high surface area as compared to other samples [59, 60].

3.12.3 Effect of dyes at different times

The degradation efficiency of $Ni_xZn_{1-x}Fe_2O_4$ (x = 0.0, 0.2, 0.4, 0.6, 0.8, and 1.0) nanoparticles under sunlight was recorded by UV–Vis spectroscopy. The maximum absorbance spectra of RhB dye at 552 nm are depicted in Fig. 13. It is shown that the absorbance spectra of $Ni_{0.8}Zn_{0.2}Fe_2O_4$ nanoparticles with RhB dyes degrade at different interval times under the sun irradiation. These results showed that $Ni_{0.8}Zn_{0.2}Fe_2O_4$ nanoparticles have a good photocatalytic activity to degrade RhB dye as compared to other samples [61, 62].

Fig. 13

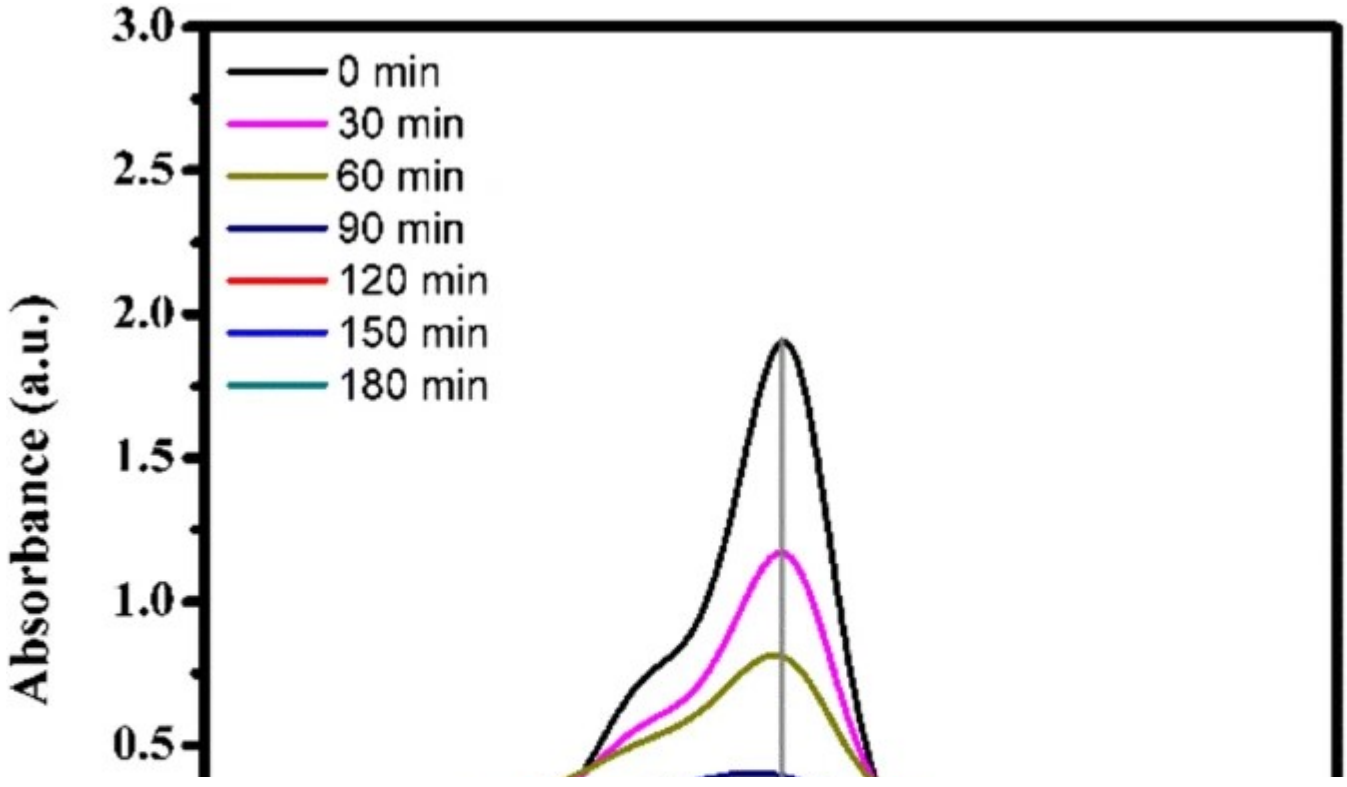

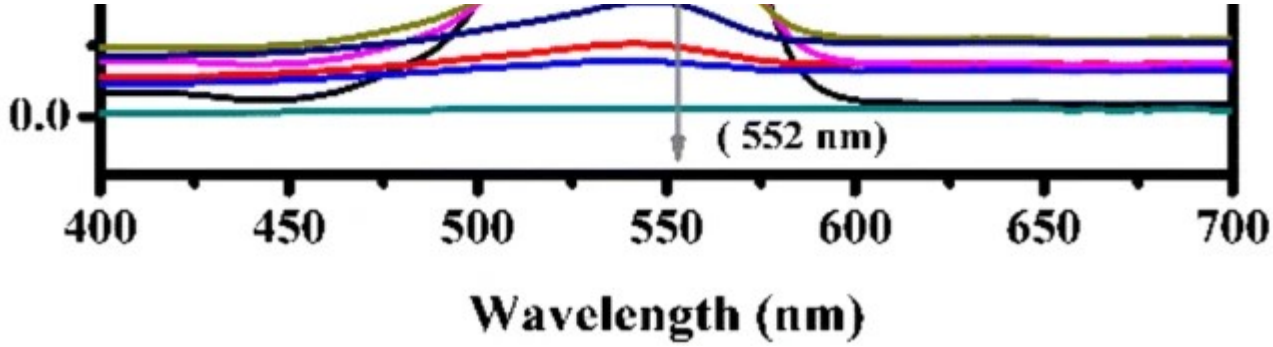

Absorbance spectra of $Ni_{0.8}Zn_{0.2}Fe_2O_4$ nanoparticles with Rhodamine B dyes under the sunlight

3.12.4 Effect of perhydroxic acid (H_2O_2) as oxidant

In Photocatalytic degradation, hydroxyl radical ($^*OH$) plays an important role in the degradation of RhB by taking perhydroxic acid, which performs as oxidant. The rate of degradation increases due to the decomposition of hydrogen peroxide in the creation of hydroxyl radical by e^-/h^+ pair recombination on the surface of the prepared samples. The e^- created in the reaction are directly reacted by Fe^{3+} with perhydroxic acid to form Fe^{2+}, which react with Perhydroxic acid to form hydroxyl radical [53]. The nanoparticles with higher surface area increases the e^-/h^+ pair recombination rate.

3.12.5 Role of active species and Mechanism of RhB with Ni–Zn nanoparticles

The effect of different scavengers on the photocatalytic reaction is shown in Fig. 14a. The trapping experiment was carried out using ethylenediaminetetraacetic acid disodium (EDTA) and isopropanol (IPA) as an O_2^-, h^+, $^*OH$ scavengers separately [63]. It was observed that the EDTA and IPA reduces the degradation efficiency of RhB. The result shows that the O^- and OH^- radicals are the active species for the dye degradation process under the sun irradiation [64]. The holes do not add to the degradation process and does not impact dye degradation reaction time. The trapping experiment was well coordinated with the overreaction mechanism.

Fig. 14

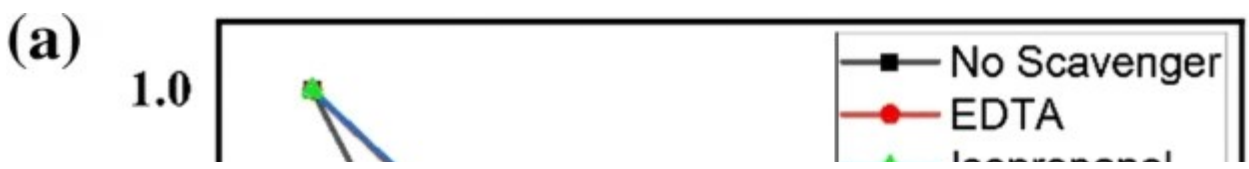

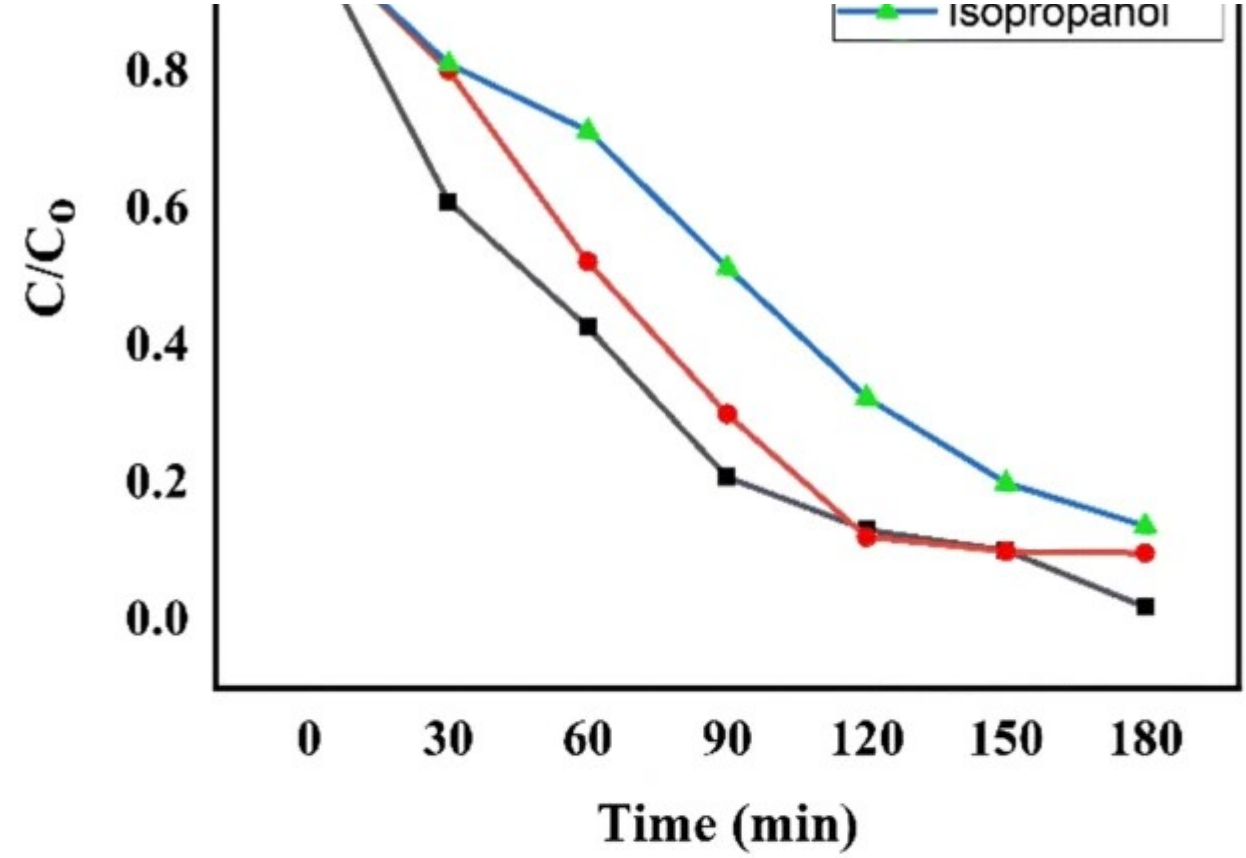

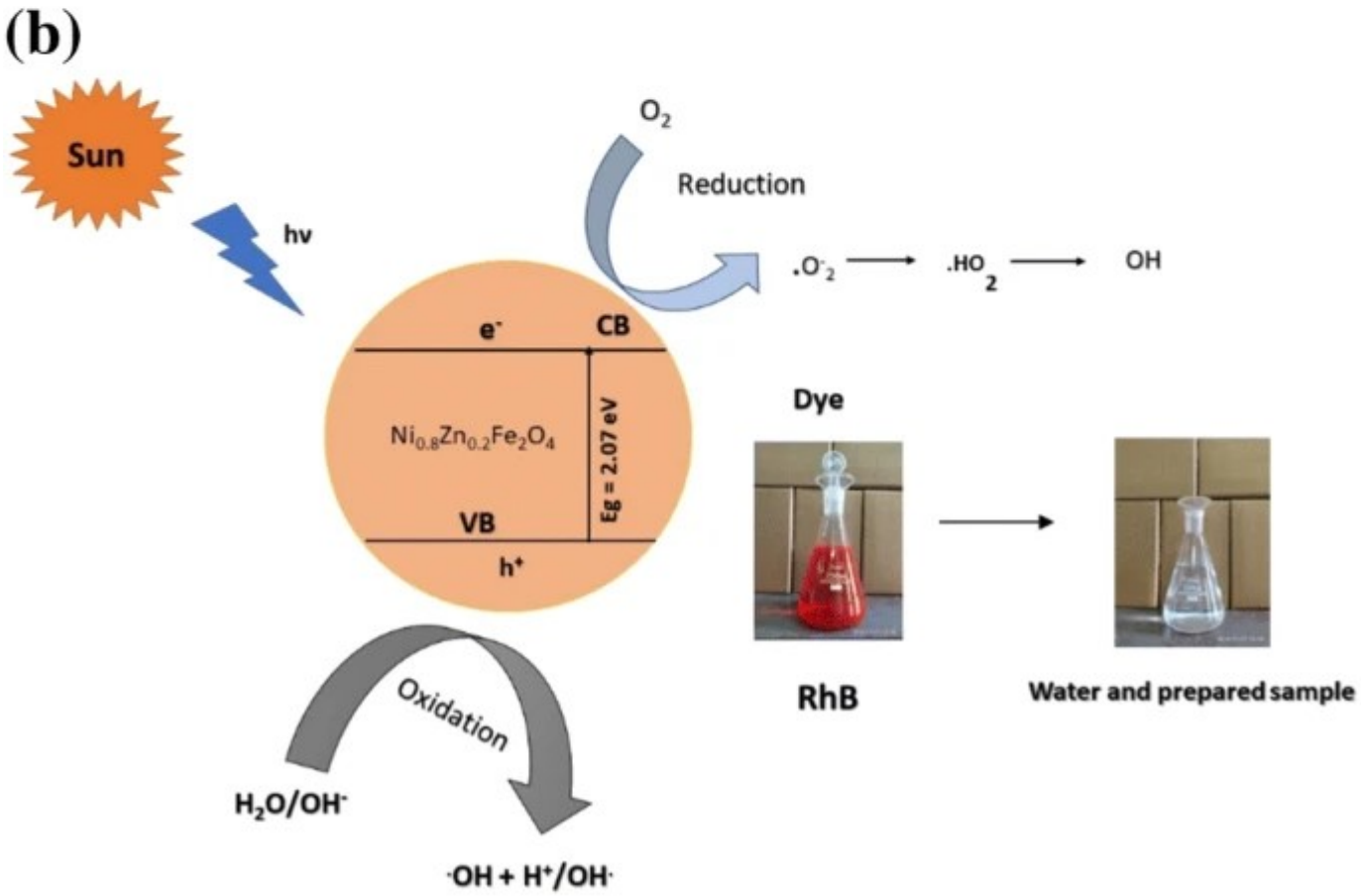

a Photocatalytic activity of $Ni_{0.8}Zn_{0.2}Fe_2O_4$ nanoparticles under the different scavengers. b Mechanism of dye degradation

The photocatalytic degradation mechanism for the degradation of RhB under the sunlight was carried out in the following equation [65,66,67,68,69,70],

$$\begin{aligned} & {\text{Ni}}_{0.8} {\text{Zn}}_{0.2} {\text{Fe}}_{2} {\text{O}}_{4} + h\nu \to {\text{h}}^{ + } + e^{ - } \\ & {\text{Ni}}_{0.8} {\text{Zn}}_{0.2} {\text{Fe}}_{2} {\text{O}}_{4} + {\text{H}}_{2} {\text{O}} \to {\text{H}}^{ + } + {\text{OH}} \\ & {\text{Ni}}_{0.8} {\text{Zn}}_{0.2} {\text{Fe}}_{2} {\text{O}}_{4} + {\text{OH}} \to {\text{OH}}^{*} \\ & {\text{Ni}}_{0.8} {\text{Zn}}_{0.2} {\text{Fe}}_{2} {\text{O}}_{4} + {\text{O}}_{2} \to {\text{O}}_{2}^{ - *} \\ & {\text{O}}_{2} + {\text{H}}^{ + } \to {\text{H}}_{2} {\text{O}} \\ & {\text{Ni}}_{0.8} {\text{Zn}}_{0.2} {\text{Fe}}_{2} {\text{O}}_{4} + {\text{H}}_{2} {\text{O}}^{ \circ } + {\text{H}}^{ + } \to {\text{H}}_{2} {\text{O}}_{2} \\ & {\text{RhB}}\,{\text{dye}} +^{ \circ } {\text{OH}} + {\text{H}}^{ + } +^{ - } {\text{O}}_{2}^{ \circ } \to {\text{CO}}_{2} + {\text{Water}} \\ \end{aligned}$$

When photocatalytic $Ni_{0.8}Zn_{0.2}Fe_2O_4$ nanoparticles absorb sunlight radiation, it will produce a pair of electron and hole (h^+/e^-). The electron of the valence band becomes excited by undergoing the sunlight irradiation. The additional energy of the excited electron promotes the electron to the conduction band of the Ni–Zn ferrite by creating h^+/e^- pair. The positive hole of Ni–Zn ferrite breaks apart the water molecules to form hydroxyl radicals. The e^- reacts with oxygen molecules to form superoxide anion and generate H_2O_2. Hence, these ions simply spell the RhB dye molecules and give rise to by-product. This is known as a redox reaction. Figure 14b shows the mechanism of RhB dye in the presence of $Ni_{0.8}Zn_{0.2}Fe_2O_4$ nanoparticles.

3.12.6 Recyclability studies

In the photocatalytic activity, recyclability of the nanoparticles is important for their active environmental and industrial applications [71, 72]. In the present studies, Ni0.8Zn0.8Fe2O4 nanoparticles were successfully recycled for five runs and its effect on dye degradation percentage is shown in Fig. 15. It shows that nanoparticle samples can be easily separated from water and reused for active degradation purposes.

Fig. 15

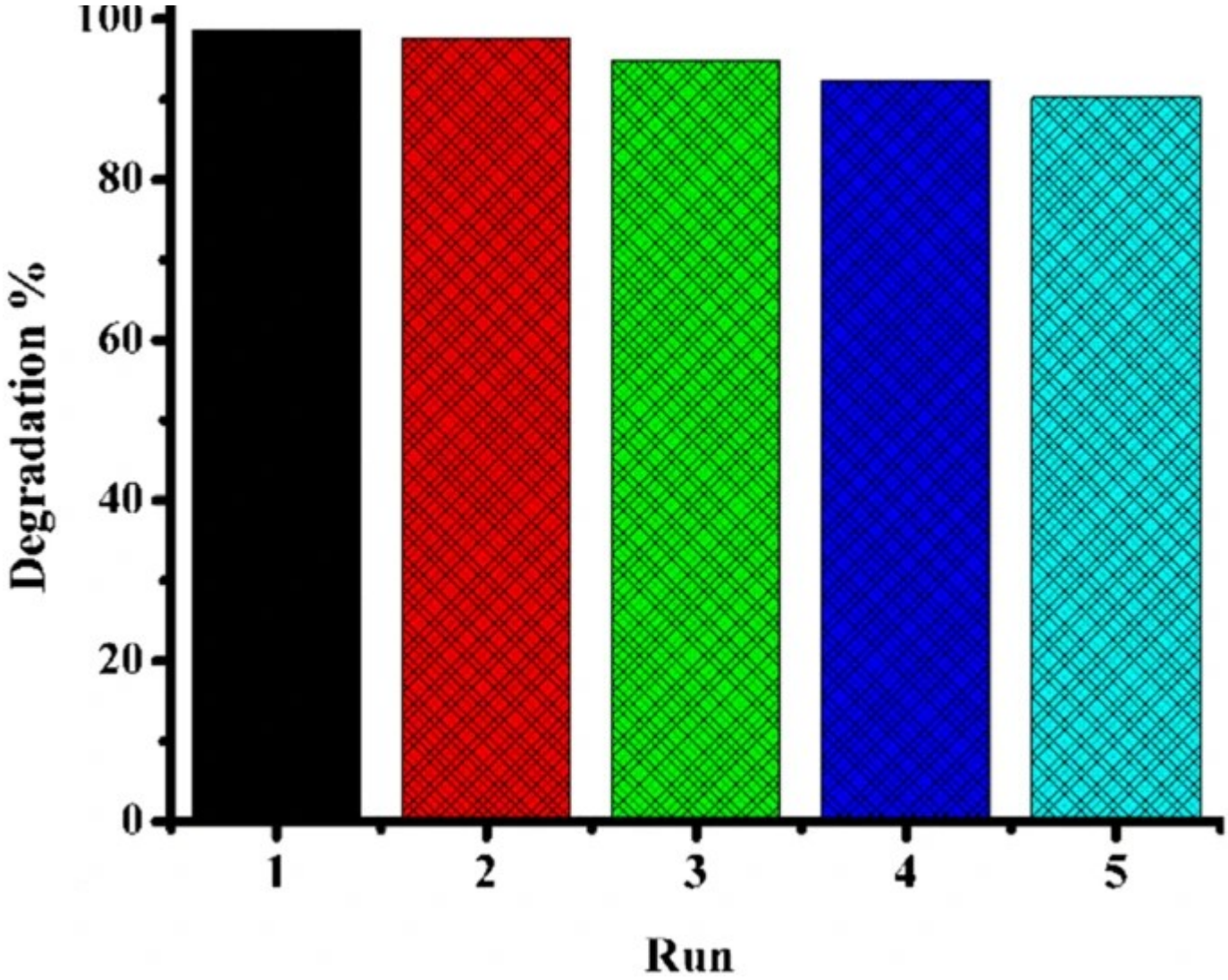

Recyclability of Ni0.8Zn0.8Fe2O4 nanoparticle

4 Conclusions

A series of mixed spinel ferrite nanoparticles ($Ni_xZn_{1-x}Fe_2O_4$, where x = 0.0, 0.2, 0.4, 0.6, 0.8, 1.0) were successfully prepared by sol–gel auto-combustion method using urea as a fuel. XRD, FT-IR, FE-SEM, EDAX, and TEM analyses confirmed the formation of nanocrystalline nanoparticles with a single-phase spinel structure. The average crystallite size was found in the range of 23 nm to 15 nm. Magnetic properties show saturation magnetization (M_s) value increased with increasing Ni^{2+} concentration with the highest value of 42.26 emu/g for $NiFe_2O_4$. The photocatalytic activity for the photodegradation of Rhodamine B was evaluated under the Sunlight irradiation successfully. $Ni_{0.8}Zn_{0.2}Fe_2O_4$ nanoparticles showed high

degradation efficiency of the order of 98.48% as compared with the other samples.

References

1. R. Tanwar, U.K. Mandal, Photocatalytic activity of $Ni_{0.5}Zn_{0.5}Fe_2O_4$@ polyaniline decorated BiOCl for azo dye degradation under visible light—integrated role and degradation kinetics interpretation. RSC Adv. 9, 8977–8993 (2019)

CAS Google Scholar

2. R. Shi, Y. Zhang, X. Wang, Q. Ma, A. Zhang, P. Yang, Electrospun $ZnFe_2O_4$ nanotubes and nanobelts: morphology evolution, formation mechanism and Fenton-like photocatalytic activities. Mater. Chem. Phys. 207, 114–122 (2018)

CAS Google Scholar

3. C. Liang, C.-G. Niu, L. Zhang, X.-J. Wen, S.-F. Yang, H. Guo, G.-M. Zeng, Construction of 2D heterojunction system with enhanced photocatalytic performance: plasmonic Bi and reduced graphene oxide co-modified Bi_5O_7I with high-speed charge transfer channels. J. Hazard. Mater. 361, 245–258 (2019)

CAS Google Scholar

4. G. Sharma, D.D. Dionysiou, S. Sharma, A. Kumar, H. Ala'a, M. Naushad, F.J. Stadler, Highly efficient Sr/Ce/activated carbon bimetallic nanocomposite for photoinduced degradation of rhodamine B. Catal. Today 335, 491–500 (2019)

Google Scholar

5. M. Ismail, K. Akhtar, M. Khan, T. Kamal, M.A. Khan, A.M. Asiri, J. Seo, S.B. Khan, Pollution, toxicity and carcinogenicity of organic dyes and their catalytic bio-remediation. Curr. Pharm. Des. 25, 3645–3663 (2019)

CAS Google Scholar

6. M.M. Naik, H.B. Naik, G. Nagaraju, M. Vinuth, K. Vinu, R. Viswanath, Green synthesis of zinc doped cobalt ferrite nanoparticles: structural, optical, photocatalytic and antibacterial studies. Nano-Struct. Nano-Objects 19, 100322 (2019)

Google Scholar

7. T. Yao, H. Wang, Q. Zuo, J. Wu, X. Zhang, F. Cui, T. Cui, One step preparation of reduced graphene oxide/Pd–Fe_3O_4@ polypyrrole composites and their application in catalysis. Chemistry 10, 1940–1947 (2015)

CAS Google Scholar

8. A. Ivanets, M. Roshchina, V. Srivastava, V. Prozorovich, T. Dontsova, S. Nahirniak, V. Pankov, A. Hosseini-Bandegharaei, H.N. Tran, M. Sillanpää, Effect of metal ions adsorption on the efficiency of methylene blue degradation onto $MgFe_2O_4$ as Fenton-like catalysts. Colloids Surf. A 571, 17–26 (2019)

CAS Google Scholar

9. P. Samoila, C. Cojocaru, L. Sacarescu, P.P. Dorneanu, A.-A. Domocos, A. Rotaru, Remarkable catalytic properties of rare-earth doped nickel ferrites synthesized by sol-gel auto-combustion with maleic acid as fuel for CWPO of dyes. Appl. Catal. B 202, 21–32 (2017)

CAS Google Scholar

10. K.K. Kefeni, B.B. Mamba, T.A. Msagati, Application of spinel ferrite nanoparticles in water and wastewater treatment: a review. Sep. Purif. Technol. 188, 399–422 (2017)

CAS Google Scholar

11. H. Kardile, S.B. Somvanshi, A.R. Chavan, A. Pandit, K. Jadhav, Effect of Cd^{2+} doping on structural, morphological, optical, magnetic and wettability properties of nickel ferrite thin films. Optik 207, 164462 (2020)

CAS Google Scholar

12. S.B. Somvanshi, M.V. Khedkar, P.B. Kharat, K. Jadhav, Influential diamagnetic magnesium (Mg^{2+}) ion substitution in nano-spinel zinc ferrite ($ZnFe_2O_4$): thermal, structural, spectral, optical and physisorption analysis. Ceram. Int. 46, 8640–8650 (2020)

CAS Google Scholar

13. M. Babrekar, K. Jadhav, Synthesis and characterization of spray deposited lithium ferrite thin film. Int. Res. J. Sci. Eng. Special 1, 73–76 (2017)

Google Scholar

14. A. Bajorek, C. Berger, M. Dulski, P. Łopadczak, M. Zubko, K. Prusik, M. Wojtyniak, A. Chrobak, F. Grasset, N. Randrianantoandro, Microstructural and magnetic characterization of $Ni_{0.5}Zn_{0.5}Fe_2O_4$ ferrite nanoparticles. J. Phys. Chem. Solids 129, 1–21 (2019)

CAS Google Scholar

15. P.B. Kharat, S.B. Somvanshi, J.S. Kounsalye, S.S. Deshmukh, P.P. Khirade, K. Jadhav, Temperature dependent viscosity of cobalt ferrite/ethylene glycol ferrofluids, in: *AIP Conference Proceedings*, AIP Publishing LLC, 2018, p. 050044.

16. S.B. Kale, S.B. Somvanshi, M. Sarnaik, S. More, S. Shukla, K. Jadhav, Enhancement in surface area and magnetization of $CoFe_2O_4$ nanoparticles for targeted drug delivery application, in: *AIP Conference Proceedings*, AIP Publishing LLC, 2018, p. 030193.

17. S.B. Somvanshi, S.R. Patade, D.D. Andhare, S.A. Jadhav, M.V. Khedkar, P.B. Kharat, P.P. Khirade, K. Jadhav, Hyperthermic evaluation of oleic acid coated nano-spinel magnesium ferrite: enhancement via hydrophobic-to-hydrophilic surface transformation. J. Alloys Compd. 835, 155422 (2020)

CAS Google Scholar

18. S.B. Somvanshi, P.B. Kharat, T.S. Saraf, S.B. Somwanshi, S.B. Shejul, K.M. Jadhav, Multifunctional nano-magnetic particles assisted viral RNA-extraction protocol for potential detection of COVID-19. Mater. Res. Innov. 1, 6 (2020)

Google Scholar

19. M. Sugimoto, The past, present, and future of ferrites. J. Am. Ceram. Soc. 82, 269–280 (1999)

CAS Google Scholar

20. Y.I. Kim, D. Kim, C.S. Lee, Synthesis and characterization of $CoFe_2O_4$ magnetic nanoparticles prepared by temperature-controlled coprecipitation method. Phys. B 337, 42–51 (2003)

CAS Google Scholar

21. S.R. Patade, D.D. Andhare, S.B. Somvanshi, P.B. Kharat, S.D. More, K.M. Jadhav, Preparation and characterisations of magnetic nanofluid of zinc ferrite for hyperthermia. Nanomater. Energy 9, 1–6 (2020)

Google Scholar

22. V. Bhagwat, A.V. Humbe, S. More, K. Jadhav, Sol-gel auto combustion synthesis and characterizations of cobalt ferrite nanoparticles: different fuels approach. Mater. Sci. Eng. B 248, 114388 (2019)

CAS Google Scholar

23. S.B. Somvanshi, R.V. Kumar, J.S. Kounsalye, T.S. Saraf, K. Jadhav, Investigations of structural, magnetic and induction heating properties of surface functionalized zinc ferrite nanoparticles for hyperthermia applications, in: *AIP Conference Proceedings*, AIP Publishing LLC, 2019, p. 030522.

24. A. Bhosale, S.B. Somvanshi, V. Murumkar, K. Jadhav, Influential incorporation of RE metal ion (Dy^{3+}) in yttrium iron garnet (YIG) nanoparticles: magnetic, electrical and dielectric behaviour. Ceram. Int. (2020). https://doi.org/10.1016/j.ceramint.2020.03.081

Article Google Scholar

25. N.D. Raskar, D.V. Dake, V.A. Mane, E. Stathatos, U. Deshpande, B. Dole, One step synthesis of vertically grown Mn-doped ZnO nanorods for photocatalytic application. J. Mater. Sci. Mater. Electron. 30, 10886–10899 (2019)

CAS Google Scholar

26. F. Zhan, R. Wang, J. Yin, Z. Han, L. Zhang, T. Jiao, J. Zhou, L. Zhang, Q. Peng, Facile solvothermal preparation of Fe_3O_4–Ag nanocomposite with excellent catalytic performance. RSC Adv. 9, 878–883 (2019)

CAS Google Scholar

27. A. Gedanken, Y. Nitzan, I. Perelshtein, N. Perkas, G. Applerot, Sonochemical coating of textiles with metal oxide nanoparticles for antimicrobial fabrics. Google Patents, 2019.

28. D. Ponnamma, J.-J. Cabibihan, M. Rajan, S.S. Pethaiah, K. Deshmukh, J.P. Gogoi, S.K. Pasha, M.B. Ahamed, J. Krishnegowda, B. Chandrashekar, Synthesis, optimization and applications of ZnO/polymer nanocomposites. Mater. Sci. Eng. C 98, 1210–1240 (2019)

CAS Google Scholar

29. D.N. Bhoyar, S.B. Somvanshi, P.B. Kharat, A. Pandit, K. Jadhav, Structural, infrared, magnetic and ferroelectric properties of $Sr_{0.5}Ba_{0.5}Ti_{1-x}Fe_xO_3$ nanoceramics: modifications via trivalent Fe ion doping. Phys. B 581, 411944 (2020)

CAS Google Scholar

30. P. Sivakumar, R. Ramesh, A. Ramanand, S. Ponnusamy, C. Muthamizhchelvan, Synthesis and characterization of $NiFe_2O_4$ nanoparticles and nanorods. J. Alloys Compd. 563, 6–11 (2013)

CAS Google Scholar

31. I.J.C. Lynda, M. Durka, A. Dinesh, A. Manikandan, S. Jaganathan, A. Baykal, S.A. Antony, Enhanced magneto-optical and photocatalytic properties of ferromagnetic $Mg_{1-y}Ni_yFe_2O_4$ ($0.0 \le y \le 10$) spinel nano-ferrites. J. Supercond. Novel Magn. 31, 3637–3647 (2018)

CAS Google Scholar

32. P. Hankare, K. Sanadi, K. Garadkar, D. Patil, I. Mulla, Synthesis and characterization of

nickel substituted cobalt ferrite nanoparticles by sol–gel auto-combustion method. J. Alloys Compd. 553, 383–388 (2013)

CAS Google Scholar

33. M.V. Khedkar, S.B. Somvanshi, A.V. Humbe, K. Jadhav, Surface modified sodium silicate based superhydrophobic silica aerogels prepared via ambient pressure drying process. J. Non-Cryst. Solids 511, 140–146 (2019)

CAS Google Scholar

34. P. Sivakumar, R. Ramesh, A. Ramanand, S. Ponnusamy, C. Muthamizhchelvan, Preparation and properties of nickel ferrite ($NiFe_2O_4$) nanoparticles via sol–gel auto-combustion method. Mater. Res. Bull. 46, 2204–2207 (2011)

CAS Google Scholar

35. L. Satyanarayana, K.M. Reddy, S.V. Manorama, Nanosized spinel $NiFe_2O_4$: a novel material for the detection of liquefied petroleum gas in air. Mater. Chem. Phys. 82, 21–26 (2003)

CAS Google Scholar

36. S.B. Somvanshi, P.B. Kharat, M.V. Khedkar, K. Jadhav, Hydrophobic to hydrophilic surface transformation of nano-scale zinc ferrite via oleic acid coating: magnetic hyperthermia study towards biomedical applications. Ceram. Int. 46, 7642–7653 (2020)

CAS Google Scholar

37. C. Muntean, M. Bozdog, S. Duma, M. Stefanescu, Study on the formation of $Co_{1-x}Zn_xFe_2O_4$ system using two low-temperature synthesis methods. J. Therm. Anal. Calorim. 123, 117–126 (2016)

CAS Google Scholar

38. P.B. Kharat, S. More, S.B. Somvanshi, K. Jadhav, Exploration of thermoacoustics behavior of water based nickel ferrite nanofluids by ultrasonic velocity method. J. Mater. Sci. Mater. Electron. 30, 6564–6574 (2019)

CAS Google Scholar

39. V. Bharati, S.B. Somvanshi, A.V. Humbe, V. Murumkar, V. Sondur, K. Jadhav, Influence of trivalent Al–Cr co-substitution on the structural, morphological and Mössbauer properties of nickel ferrite nanoparticles. J. Alloys Compd. 821, 153501 (2020)

CAS Google Scholar

40. H. Mohseni, H. Shokrollahi, I. Sharifi, K. Gheisari, Magnetic and structural studies of the Mn-doped Mg–Zn ferrite nanoparticles synthesized by the glycine nitrate process. J. Magn. Magn. Mater. 324, 3741–3747 (2012)

CAS Google Scholar

41. S. Joshi, M. Kumar, S. Chhoker, G. Srivastava, M. Jewariya, V. Singh, Structural, magnetic, dielectric and optical properties of nickel ferrite nanoparticles synthesized by co-precipitation method. J. Mol. Struct. 1076, 55–62 (2014)

CAS Google Scholar

42. M.V. Khedkar, S.A. Jadhav, S.B. Somvanshi, P.B. Kharat, K. Jadhav, Physicochemical properties of ambient pressure dried surface modified silica aerogels: effect of pH variation. SN Appl. Sci. 2, 1–10 (2020)

Google Scholar

43. S.B. Somvanshi, S.A. Jadhav, M.V. Khedkar, P.B. Kharat, S. More, K. Jadhav, Structural, thermal, spectral, optical and surface analysis of rare earth metal ion (Gd^{3+}) doped mixed Zn–Mg nano-spinel ferrites. Ceram. Int. (2020). https://doi.org/10.1016/j.ceramint.2020.02.091

Article Google Scholar

44. P.A. Vinosha, B. Xavier, D. Anceila, S.J. Das, Nanocrystalline ferrite (MFe_2O_4, M= Ni, Cu, Mn and Sr) photocatalysts synthesized by homogeneous co-precipitation technique. Optik 157, 441–448 (2018)

CAS Google Scholar

45. F.R. Mariosi, J. Venturini, A. da Cas Viegas, C.P. Bergmann, Lanthanum-doped spinel cobalt ferrite ($CoFe_2O_4$) nanoparticles for environmental applications. Ceram. Int. 45, 22316–22323 (2019)

Google Scholar

46. G. Zhou, Z. Ren, L. Wang, J. Wu, B. Sun, A. Zhou, G. Zhang, S. Zheng, S. Duan, Q. Song, Resistive switching memory integrated with amorphous carbon-based nanogenerators for self-powered device. Nano Energy 63, 103793 (2019)

CAS Google Scholar

47. L. Wu, T.-S. Wu, C.-C. Wei, Effects of various substitutions on the DC resistivity of ferrites. J. Phys. D 13, 259 (1980)

CAS Google Scholar

48. B. Sun, X. Zhang, G. Zhou, C. Zhang, P. Li, Y. Xia, Y. Zhao, Effect of Cu ions assisted conductive filament on resistive switching memory behaviors in $ZnFe_2O_4$-based devices.

J. Alloys Compd. 694, 464–470 (2017)

CAS Google Scholar

49. W. Hu, X. Chen, G. Wu, Y. Lin, N. Qin, D. Bao, Bipolar and tri-state unipolar resistive switching behaviors in Ag/$ZnFe_2O_4$/Pt memory devices. Appl. Phys. Lett. 101, 063501 (2012)

Google Scholar

50. C. Murugesan, G. Chandrasekaran, Impact of Gd^{3+} substitution on the structural, magnetic and electrical properties of cobalt ferrite nanoparticles. RSC Adv. 5, 73714–73725 (2015)

CAS Google Scholar

51. O. Hemeda, M. El-Saadawy, Effect of gamma irradiation on the structural properties and diffusion coefficient in Co–Zn ferrite. J. Magn. Magn. Mater. 256, 63–68 (2003)

CAS Google Scholar

52. A.V. Humbe, A.C. Nawle, A. Shinde, K. Jadhav, Impact of Jahn Teller ion on magnetic and semiconducting behaviour of Ni-Zn spinel ferrite synthesized by nitrate-citrate route. J. Alloys Compd. 691, 343–354 (2017)

CAS Google Scholar

53. Z. Ambrus, N. Balázs, T. Alapi, G. Wittmann, P. Sipos, A. Dombi, K. Mogyorósi, Synthesis, structure and photocatalytic properties of Fe (III)-doped TiO_2 prepared from TiCl3. Appl. Catal. B 81, 27–37 (2008)

CAS Google Scholar

54. T. Takagahara, K. Takeda, Theory of the quantum confinement effect on excitons in quantum dots of indirect-gap materials. Phys. Rev. B 46, 15578 (1992)

CAS Google Scholar

55. H.J. Krug, L. Pohlmann, L. Kuhnert, Analysis of the modified complete Oregonator accounting for oxygen sensitivity and photosensitivity of Belousov-Zhabotinskii systems. J. Phys. Chem. 94, 4862–4866 (1990)

CAS Google Scholar

56. K. Zipare, S. Bandgar, G. Shahane, Effect of Dy-substitution on structural and magnetic properties of MnZn ferrite nanoparticles. J. Rare Earths 36, 86–94 (2018)

CAS Google Scholar

57. G. Padmapriya, A. Manikandan, V. Krishnasamy, S.K. Jaganathan, S.A. Antony, Spinel $Ni_xZn_{1-x}Fe_2O_4$ ($0.0 \leq x \leq 1.0$) nano-photocatalysts: synthesis, characterization and photocatalytic degradation of methylene blue dye. J. Mol. Struct. 1119, 39–47 (2016)

CAS Google Scholar

58. G. Padmapriya, A. Manikandan, V. Krishnasamy, S.K. Jaganathan, S.A. Antony, Enhanced catalytic activity and magnetic properties of spinel $Mn_xZn_{1-x}Fe_2O_4$ ($0.0 \leq x \leq 1.0$) nano-photocatalysts by microwave irradiation route. J. Supercond. Novel Magn. 29, 2141–2149 (2016)

CAS Google Scholar

59. G. Mathubala, A. Manikandan, S. Arul-Antony, P. Ramar, Enhanced photocatalytic activity of spinel $Cu_xMn_{1-x}Fe_2O_4$ nanocatalysts for the degradation of methylene blue dye and opto-magnetic properties. Nanosci. Nanotechnol. Lett. 8, 375–381 (2016)

Google Scholar

60. B. Chethan, Y. Ravikiran, S. Vijayakumari, H. Rajprakash, S. Thomas, Nickel substituted cadmium ferrite as room temperature operable humidity sensor. Sens. Actuators A 280, 466–474 (2018)

CAS Google Scholar

61. V. Chaudhary, R. Chaudhary, Magnetic nanoparticles: synthesis, functionalization, and applications. Nanosci. Nanotechnol. 28, 153–183 (2018)

Google Scholar

62. D. Moitra, Development of novel synthetic methodologies for the preparation of multifunctional ferrite reduced graphene oxide nanocomposites and study of their microwave absorption and catalytic properties (2018).

63. J. Lv, Q. Hu, C. Cao, Y. Zhao, Modulation of valence band maximum edge and photocatalytic activity of BiO_X by incorporation of halides. Chemosphere 191, 427–437 (2018)

CAS Google Scholar

64. B. Palanivel, C. Ayappan, V. Jayaraman, S. Chidambaram, R. Maheswaran, A. Mani, Inverse spinel $NiFe_2O_4$ deposited g-C_3N_4 nanosheet for enhanced visible light photocatalytic activity. Mater. Sci. Semicond. Process. 100, 87–97 (2019)

CAS Google Scholar

65. P.G. Bruce, B. Scrosati, J.M. Tarascon, Nanomaterialien für wiederaufladbare Lithiumbatterien. Angew. Chem. 120, 2972–2989 (2008)

Google Scholar

66. S.H. Im, U. Jeong, Y. Xia, Polymer hollow particles with controllable holes in their surfaces. Nat. Mater. 4, 671–675 (2005)

Google Scholar

67. X.Y. Chen, C. Ma, S.P. Bao, Z. Li, Synthesis and photoluminescence of $ZnAl_2O_4$: Eu^{3+} hollow nanophosphors using carbon nanospheres as hard templates. J. Colloid Interface Sci. 346, 8–11 (2010)

CAS Google Scholar

68. C. Wang, Y. Ao, P. Wang, J. Hou, J. Qian, S. Zhang, Preparation, characterization, photocatalytic properties of titania hollow sphere doped with cerium. J. Hazard. Mater. 178, 517–521 (2010)

CAS Google Scholar

69. V. Valtchev, Silicalite-1 hollow spheres and bodies with a regular system of macrocavities. Chem. Mater. 14, 4371–4377 (2002)

CAS Google Scholar

70. A. Dinsmore, M.F. Hsu, M. Nikolaides, M. Marquez, A. Bausch, D. Weitz, Colloidosomes: selectively permeable capsules composed of colloidal particles. Science 298, 1006–1009 (2002)

CAS Google Scholar

71. Y. Chen, F. Li, W. Cao, T. Li, Preparation of recyclable CdS photocatalytic and superhydrophobic films with photostability by using a screen-printing technique. J.

Mater. Chem. A 3, 16934–16940 (2015)

CAS Google Scholar

72. R.M. Borade, S.B. Somvanshi, S.B. Kale, R.P. Pawar, K. Jadhav, Spinel zinc ferrite nanoparticles: an active nanocatalyst for microwave irradiated solvent free synthesis of chalcones. Mater. Res. Express 7, 016116 (2020)

CAS Google Scholar

Acknowledgements

The author SAJ acknowledges Prof. B.N. Dole, Department of Physics, Dr. B. A. M. University and Head, Department of Chemistry, Dr. B. A. M. University for providing UV–Vis and FT-IR measurements, respectively. Author Sandeep B. Somvanshi acknowledges Department of Science and Technology (DST), Government of India for DST-INSPIRE Fellowship (IF170288).

Author information

Authors and Affiliations

Department of Physics, Dr. Babasaheb Ambedkar Marathwada University, Aurangabad, Maharashtra, 431004, India

Swapnil A. Jadhav, Sandeep B. Somvanshi, Mangesh V. Khedkar, Supriya R. Patade & K. M. Jadhav

Corresponding author

Correspondence to K. M. Jadhav.

Ethics declarations

Conflict of interest

No conflict of interest associated with this work.

Additional information

Publisher's Note

Rights and permissions

About this article

Cite this article

Jadhav, S.A., Somvanshi, S.B., Khedkar, M.V. *et al.* Magneto-structural and photocatalytic behavior of mixed Ni–Zn nano-spinel ferrites: visible light-enabled active photodegradation of rhodamine B. *J Mater Sci: Mater Electron* 31, 11352–11365 (2020). https://doi.org/10.1007/s10854-020-03684-1

Received
12 December 2019

Accepted
25 May 2020

Published
31 May 2020

Issue Date
July 2020

DOI
https://doi.org/10.1007/s10854-020-03684-1

Share this article

Anyone you share the following link with will be able to read this content:

Get shareable link